

MECHANICAL AND MAGNETIC PROPERTIES OF GLASS COATED
AMORPHOUS METAL FIBERS

BY

BRIAN P. DOUD

A THESIS
SUBMITTED TO THE FACULTY OF

ALFRED UNIVERSITY

IN PARTIAL FULFILLMENT OF THE REQUIREMENTS
FOR THE DEGREE OF

MASTER OF SCIENCE

IN

MATERIALS SCIENCE AND ENGINEERING

ALFRED, NEW YORK

JUNE, 2004

Alfred University theses are copyright protected and may be used for education or personal research only. Reproduction or distribution in part or whole is prohibited without written permission from the author.

MECHANICAL AND MAGNETIC PROPERTIES OF GLASS COATED
AMORPHOUS METAL FIBERS

BY

BRIAN P. DOUD

B.S. ALFRED UNIVERSITY (2002)

SIGNATURE OF AUTHOR _____ (Signature on file)

APPROVED BY _____ (Signature on file)

WILLIAM LaCOURSE, ADVISOR

(Signature on file)

MATTHEW HALL, ADVISORY COMMITTEE

(Signature on file)

WILLIAM CARLSON, ADVISORY COMMITTEE

(Signature on file)

DOREEN EDWARDS, CHAIR, ORAL THESIS DEFENSE

ACCEPTED BY _____ (Signature on file)

ALASTAIR CORMACK, DEAN,
SCHOOL OF ENGINEERING

ACKNOWLEDGMENTS

I would like to thank my advisor, Dr. William C. LaCourse, for listening to my “interesting” ideas and pointing me in the right direction. My thanks goes out to Dr. William Carlson for always having a million more ideas for me if one did not work out. I thank Dr. Matthew Hall, Dr. Arun Varshneya and Dr. Linda Jones for their conversations ideas and help along the way.

I would like especially like to thank my parents for always pushing me to do what ever I wanted to do and always supporting my decisions.

I thank all of my friends here at Alfred because with out you this town would be a dreadfully boring place indeed.

TABLE OF CONTENTS

	Page
Acknowledgments	iii
Table of Contents.....	iv
List of Tables.....	vi
List of Figures.....	vii
Abstract.....	x
I INTRODUCTION.....	1
A. Manufacture of GCAF.....	1
B. Mechanical properties of GCAF	2
1. Composite structure.....	2
2. Internal stress	3
C. Magnetic properties of and sensing applications of GCAF	5
1. Magnetostriction and MDL.....	5
2. LBE	6
3. GMI.....	6
4. Magnetic permeability.....	6
II EXPERIMENTAL PROCEDURE.....	7
A. Samples.....	7
1. Sample preparation.....	7
B. Analysis	8
1. Tensile testing.....	8
2. Elastic modulus analysis.....	10
3. Optical microscopy.....	11
4. SEM.....	11
C. Magnetic sensor	11
1. Construction.....	12
2. Testing.....	13
a. Tension sensor	14
b. Torsion sensor.....	14
3. Finite element analysis	14
III RESULTS AND DISCUSSION.....	15
A. Mechanical properties.....	15

1.	Tensile	15
2.	Elastic modulus	18
3.	Mode of failure.....	21
	a. CoFeSiB	23
	b. CoFeNiSiB.....	25
	c. FeSiB.....	28
B.	Heat treatments	29
C.	Magnetic properties	30
	1. Harmonics.....	31
	a. FeSiB.....	31
	b. CoFeSiB	34
	2. Waveform shapes (occiliscope).....	36
	a. FeSiB.....	36
	b. CoFeSiB	37
	c. CoFeNiSiB.....	39
	3. Multiple fibers and fiber size	39
	a. Multiple fibers.....	39
	b. Fiber length.....	43
D.	Mechanical and magnetic coupling.....	45
	1. Tension	45
	2. Torsion.....	49
	3. Stress relief	49
IV	SUMMARY AND CONCLUSIONS.....	52
V	FUTURE WORK	54
	REFERENCES	55

LIST OF TABLES

	Page
Table I Compositions and Specifications of As-received Fibers.....	7
Table II Tensile Strength of As-received Fibers	16
Table III Tensile Stress of Glass-removed Fibers	17
Table IV Elastic Modulus of A-R Fibers	19
Table V Elastic Modulus of G-R Fibers	20
Table VI Calculated Modulus Using Formula 1 Compared to Experimental	21
Table VII Fiber Strength after Crystallization.....	30
Table VIII Calibration Data for CoFeSiB Fibers as a Load Cell in the Sensor (Load(N)=output voltage (mV) of harmonic x slope + intercept)	47
Table IX Stress Relieved by the Removal of the Glass Coating for CoFeSiB Fibers	51

LIST OF FIGURES

	Page
Figure 1. Glass-coated melt spinning.....	2
Figure 2. Fiber tensile tester.....	9
Figure 3. Fiber sample holder for tensile testing.....	9
Figure 4. Device for modulus testing.....	10
Figure 5. Change in magnetic field $ B $ along the sensing coil as the permeability of the core material changes.....	12
Figure 6. Sensor device.....	13
Figure 7. FEMM output showing magnetic flux lines and $ B $	15
Figure 8. Comparison of the force at break between as received and glass-removed CoFeSiB fibers.....	18
Figure 9. Fracture end of a FeSiB GCAF at 980x magnification.....	22
Figure 10. Glass fracture from core after tensile failure FeSiB GCAF.....	22
Figure 11. Glass fracture for CoFeNiSiB back scattered electron image dark regions represent glass.....	23
Figure 12. Stress strain curve for CoFeSiB 4.....	23
Figure 13. Video Frames of CoFeSiB cracking under tensile load.....	25
Figure 14. Stress strain curve showing CoFeNiSiB where the glass cladding fails.....	27
Figure 15. Stress strain curve showing CoFeNiSiB where the glass cladding fails when the fiber fails.....	27

Figure 16. Video frames of CoFeNiSiB breaking under tensile load (arrow shows fracture progression).....	28
Figure 17. Stress strain Curve for FeSiB M6.	29
Figure 18. Harmonic components of FeSiB as-received fibers.....	32
Figure 19. Percentage Harmonic components of FeSiB glass-removed fibers.....	33
Figure 20. Comparison of as-received and glass-removed samples for FeSiB.	33
Figure 21. Harmonic components of CoFeSiB as-recieved fibers.	34
Figure 22. Harmonic components of CoFeSiB glass-removed fibers.	35
Figure 23. Comparison of as-received and glass-removed samples for CoFeSiB.	35
Figure 24. FeSiB M7 as received.....	36
Figure 25. FeSiB M7 glass-removed.	37
Figure 26. CoFeSiB M3 A-R.....	38
Figure 27. CoFeSiB 2 A-R fiber.....	38
Figure 28. CoFeNiSiB 4, A-R	39
Figure 29. Occsiloscope readings for multiple fibers.	40
Figure 30. Upper LH side CoFeSiB 2 upper RH side CoFeNiSiB 4. Bottom both fibers in sensor showing combined signal.	41
Figure 31. Change in output voltage for different harmonics as more CoFeSiB M1 fibers are added to the sample.	42
Figure 32. Comparison of two different CoFeSiB samples with respect to additional fibers(up to 4) in the sensor.....	42
Figure 33. Change in magnetic field at the sensing coil as fiber sample length changes.	43

Figure 34. Change in voltage output with respect to sample length for CoFeSiB 2.	44
Figure 35. Change in voltage output with respect to changing sample length for M1 CoFeSiB.	44
Figure 36. CoFeSiB fibers calibration curves for 3 rd harmonic to be used use as a load cell.	46
Figure 37. Changes in slope of CoFeSiB before (clad) and after (core) Glass removal for different harmonics.	48
Figure 38. Maximum amount of weight that can be sensed on a specific harmonic and fiber type.	48
Figure 39. Effect of torsional stress on harmonic response of G-R CoFeSiB M1.	49
Figure 40. Calculating relieved stress when glass cladding is removed.	50
Figure 41. Axial stress on the metal core as a function of area ratio using Chiriac and Rongved's formulas.	51

ABSTRACT

Mechanical properties of glass-coated metal fiber with different metal compositions ($\text{Co}_{68.15}\text{Fe}_{4.35}\text{Si}_{12.5}\text{B}_{15}$, $\text{Co}_{68.15-x}\text{Fe}_{4.35}\text{Ni}_x\text{Si}_{12.5}\text{B}_{15}$, and $\text{Fe}_{77.5}\text{Si}_{7.5}\text{B}_{15}$), diameters and glass thicknesses were analyzed. Tensile strengths and elastic modulus were measured with and without the glass coating present. Strengths on the order of 1 to 1.5 GPa have been found for as-received (A-R) GCAF and strengths on the order of 2.5 to 4 GPa have been found for the glass-removed (G-R) fibers. Elastic moduli of the composite fibers fall between 68 and 98 GPa which is 10 to 20% lower than the values calculated from a composite model. Elastic moduli of the G-R fibers range from 120 GPa to 180 GPa and depend on composition and thickness of the metal fiber. The failure mode of GCAF is dependent on fiber composition and the thickness of the glass coating. Some composite fibers fail catastrophically while others exhibit high toughness in that the glass coating fails before the metal core. The influence of crystallization on the metal core was also studied. The tensile strength of GCAF decreased 10 to 40% after crystallization. A sensor was made to observe the waveform and the harmonic components that each GCAF produced under a magnetic field. The magnetic permeability of the $\text{Co}_{68.15}\text{Fe}_{4.35}\text{Si}_{12.5}\text{B}_{15}$ and CoFeNiSiB compositions is influenced by the stress placed on them by the glass coating as well as any tension or torsion forces. This change in permeability allowed the GCAF to be used in conjunction with a sensing device to function as a load cell or torsion cell. From these measurements the axial stress relieved on the metal core from the removal of the glass cladding was calculated and found to be between 180 and 250 MPa depending on the fiber. The effects of fiber length and the multiple fibers were also observed for future reference and possible device applications.

I INTRODUCTION

The process for creating glass coated amorphous metal fibers (GCAF) was invented in the early 1970's by Wiesner and Schneider¹ in a process called glass-coated melt spinning. This process itself is derived from an earlier process by Taylor² used to produce fine metallic filaments. The process was originally used to produce amorphous fibers for electronic and magnetic applications. The main benefit to processing by glass-coated melt spinning is the ability to produce metallic cores with small diameters (10-30 μ m). Originally the glass coating was not thought to benefit or be desirable to the product so it was removed. Research on GCAF took a back stage to that of conventional amorphous fibers in the 1970s and 1980s and virtually came to a standstill when the process of in-rotating-water quenching method³ was developed for making amorphous fibers without glass coatings. During the mid 1990's GCAF regained interest in the scientific community when groups from Romania, Spain and, Moldavia renewed research.^{4,5} The new research groups capitalized on GCAF magnetic properties as well as the mechanical and protective benefits that the glass coating can offer.

A. Manufacture of GCAF

Glass-coated melt spinning generally begins with a borosilicate type glass tube that has the metallic alloy inside it. The metal is then heated by induction to its melting point which in turn softens the glass enough to be drawn. The glass is then pulled downward forming a capillary that the metal fills. The GCAF is quenched by a stream of water between the inductor and a spindle. The GCAF is then wrapped on a rotating spindle for transportation or use. The diameter of the core and the glass thickness can be tailored by adjusting the amount of alloy in the tube, the glass wall thickness, and the speed at which the glass is fed into the inductor.⁵ Figure 1 shows a graphical interpretation of the process.

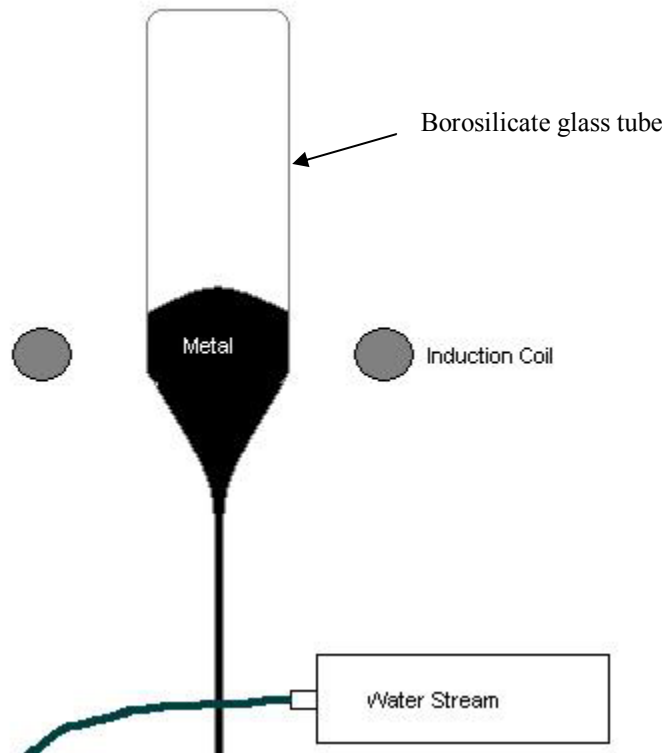


Figure 1. Glass-coated melt spinning.

B. Mechanical properties of GCAF

The mechanical properties of GCAF are not widely known and are the basis for most of this study. Amorphous metals are known to have high fracture strength approaching theoretical values of 3 to 4 GPa. The Young's modulus for amorphous metals is usually slightly lower (approximately 20%) than that of a comparable crystalline metal.⁶ Amorphous iron alloys used in the manufacture of GCAF's have been shown to have tensile strengths between 2 to 3.8 GPa with slight dependence on fiber diameter i.e. smaller diameter fibers show higher tensile strengths. The elongation of these same alloys from tensile load is usually between 2.6 and 4% at failure.⁴

1. Composite structure

GCAF consist of the metal core and the glass cladding. The mechanical properties of this type of simple composite structure depend on the volumetric ratios of the two phases, their properties, and the bonding between them. The glass cladded fibers can be thought of as a metal fiber longitudinally reinforcing a glass matrix. The critical

length (l_c) does not become a factor in calculating mechanical properties being that l_c is usually 20 to 150 times the fiber diameter ($l_c = 0.5-3.5\text{mm}$) and the fibers tested were all longer than this. Provided that the composite is continuously reinforced along the longitudinal direction and all the matrix and fiber deformations are elastic the composite upper limit for elastic modulus is given by equation 1.⁷ The bonding between the two components can affect the final properties. This equation assumes perfect bonding.

$$E_{comp} = E_m V_m + E_f V_f \quad (1)$$

The amorphous metal does not always behave elastically. However, by the time the metal exhibits plastic deformation the glass cladding should have cracked and is no longer contributing to the equation. For almost all situations where the glass has not yet cracked this reasoning holds.

2. Internal stress

During manufacture of GCAF stress arises in the metal and the glass from cooling due to a mismatch in thermal expansion coefficients. The cooling process places the glass cladding in compression and the metal core in tension. The main factors influencing the level of tension and compression in a fiber are the diameter of the core, the thickness of the cladding, the thermal expansion mismatch, elastic moduli, and cooling rates. The problem of induced stresses from the drawing of a cladded fiber is well documented. In 1980 Rongved originally provided solutions (later corrected by Varshneya) to the stresses induced in the cladding and core during a glass fiber drawing process.^{8,9} In Rongved's solution to the stress induced by drawing the contributing factors to the stress are the mismatch in thermal expansion ($\alpha_1 - \alpha_2$), the mismatch in Poisson's ratio ($\nu_2 - \nu_1$), the elastic modulus (E_1, E_2), the viscosities at drawing temperature (η_1, η_2), the respective cross sectional areas of the two phases (A_1, A_2), and the average stress placed on the fiber during drawing (σ). Equations 2-9 lead to the axial (z) radial (r) and hoop (θ) stress components for both the core and the cladding.

$$\begin{aligned}
c_1 &= \frac{(1+\nu_1)A_1 + 2A_2}{E_1A_1} + \frac{1-\nu_2}{E_2} \\
c_2 &= \frac{\nu_1}{E_1A_1} + \frac{\nu_2}{E_2A_2} \\
c_3 &= \frac{1}{E_1A_1} + \frac{1}{E_2A_2}
\end{aligned} \tag{2}$$

$$p = \frac{(c_2 + c_3)(\alpha_1 - \alpha_2)T^* A_1 A_2 E_1 E_2 + (\nu_2 - \nu_1)F}{(c_1 c_2 - 2A_2 c_2^2) A_1 A_2 E_1 E_2} \tag{3}$$

$$\sigma_r^{(1)} = \frac{A_2 p}{A_1} \left[1 - \frac{a^2}{r^2} \right] \tag{4}$$

$$\sigma_\theta^{(1)} = \frac{A_2 p}{A_1} \left[1 + \frac{a^2}{r^2} \right] \tag{5}$$

$$\sigma_z^{(1)} = \left[\frac{\eta_1}{\bar{\eta}} - \frac{E_1}{\bar{E}} \right] \bar{\sigma} \tag{6}$$

$$\sigma_r^{(2)} = -p \tag{7}$$

$$\sigma_\theta^{(2)} = -p \tag{8}$$

$$\sigma_z^{(2)} = \left[\frac{\eta_2}{\bar{\eta}} - \frac{E_2}{\bar{E}} \right] \bar{\sigma} \tag{9}$$

Where $\bar{E} = (E_1 A_1 + E_2 A_2)/A$, average viscosity ($\bar{\eta}$) follows the same argument based on area. $\bar{s} = F/A$, is the applied draw force placed on the fiber. T is the temperature at which the draw occurs. Superscript (1) designates the cladding and (2) designates the core.

Chiriac's¹⁰ approach takes in to account the difference in elastic modulus (E), thermal expansion (α) and cross sectional area (A). It does not take into account the drawing force used to pull the fiber (F). Chiriac's equations only concentrate on the stress induced in the metal.

$$S = \frac{A_1}{A_2} \quad (10)$$

$$\Psi = \frac{E_1}{E_2} \quad (11)$$

$$\varepsilon = (\alpha_2 - \alpha_1) \Delta T \quad (12)$$

$$\sigma_r^{(2)} = \sigma_\theta^{(2)} = \frac{3\Psi S}{(\Psi + 3)S + 4} \varepsilon E_2 \quad (13)$$

$$\sigma_z^{(2)} = \sigma_r^{(2)} \frac{(\Psi + 1)S + 2}{\Psi S + 1} \quad (14)$$

The two approaches give similar results for axial stress in the core especially when the stress induced by the drawing force is set constant. Both Rongved's and Chiriac's solutions are non linear with respect to the ratio between the core area and the clad area.

C. Magnetic properties and sensing applications of GCAF

GCAF as well as other amorphous metal materials have gained their popularity from a research point mainly from their magnetic properties. These properties are used to create new devices or improve on old ones.

1. Magnetostriction and MDL

Amorphous metals of various compositions are known to possess different magnetostrictive properties. Magnetostriction is the change in length in one axis of a material due to the change of a magnetic field. This property is described by the coefficient of magnetostriction (λ) value which is change in length divided by the change in magnetic field. The composition CoFeSiB is considered a zero magnetostrictive material but it actually has extremely small negative magnetostriction. FeSiB is considered a highly positive magnetostrictive material with λ values around 35×10^{-6} .⁴

The magnetostrictive delay line (MDL) technique has been used in high iron composition GCAF by Chiriac and others to measure tensile stress and torsion stress.^{11,12}

MDL uses a susceptible material like a GCAF as a core inside a coil that produces a magnetic field. The material experiences magnetostriction which causes stress that in turns produces a second magnetic field down the length of the material from the reverse magnetostriction effect that is measured by a second coil.¹³ The MDL behavior is being looked at as a less expensive rout to making transducers and multiplexers.

2. LBE

The large Barkhausen effect is a property that has been demonstrated in the FeSiB composition.^{4,14,15} The Barkhausen effect was originally found by placing a ferromagnetic substance inside a coil that was connected to a speaker through an amplifier. As a magnet or magnetic field moves along or next to the ferromagnetic substance a roaring sound is made by the speaker. The roaring sound is from the fast reorientation of the magnetic domains inside the ferromagnetic substance. This effect can be used in sensing type devices to monitor changes in the magnetic field.

3. GMI

Giant magneto-impedance (GMI) effect has been demonstrated for amorphous compositions with high Cobalt content like CoFeSiB and CoFeNiSiB.^{4,14-17} GMI is capable of sensing very small magnetic fields up to one million times smaller than the magnetic field of the earth. The GMI effect works by sensing the resistance component of the electrical impedance for a material that has this GMI quality.¹⁸ The resistance can increase dramatically (100% for the earths magnetic field) when a small magnetic field is present. This results in a very sensitive device because the resistance can be measured very accurately.

4. Magnetic permeability

It has been shown that the magnetic permeability of amorphous fibers with a high cobalt concentration changes with changes in the glass coating¹⁹ and external forces.⁴ The permeability changes due to the reorganization of domain structure in the metal from an external force. This study also looks at how tensile stress and torsion change the permeability of Co-rich GCAF's and how the glass coating influences permeability.

II EXPERIMENTAL PROCEDURE

A. Samples

Glass covered amorphous fibers (GCAF) were provided by the National Institute of R&D for Technical Physics in Romania. The fiber was packaged on spools 50-100m in length. Various diameters of fibers were studied from three different compositions. Table 1 shows the fiber designation, composition, total diameter, and core diameter of the fibers received from Romania. The three compositions are $\text{Co}_{68.15}\text{Fe}_{4.35}\text{Si}_{12.5}\text{B}_{16}$ (CoFeSiB), $\text{Co}_{68.15-x}\text{Fe}_{4.35}\text{Ni}_x\text{Si}_{12.5}\text{B}_{16}$ (CoFeNiSiB) where x is between .5 and 1, and $\text{Fe}_{77.5}\text{Si}_{7.5}\text{B}_{15}$ (FeSiB).

Table I Compositions and Specifications of As-received Fibers.

Designation	Composition	d_w (μm)	d_i (μm)
2	$\text{Co}_{68.15}\text{Fe}_{4.35}\text{Si}_{12.5}\text{B}_{16}$	24	40
3	$\text{Co}_{68.15}\text{Fe}_{4.35}\text{Si}_{12.5}\text{B}_{16}$	23	38
4	$\text{Co}_{68.15}\text{Fe}_{4.35}\text{Si}_{12.5}\text{B}_{16}$	25	39
M1	$\text{Co}_{68.15}\text{Fe}_{4.35}\text{Si}_{12.5}\text{B}_{16}$	24	40
M3	$\text{Co}_{68.15}\text{Fe}_{4.35}\text{Si}_{12.5}\text{B}_{16}$	25	40
M4	$\text{Co}_{68.15}\text{Fe}_{4.35}\text{Si}_{12.5}\text{B}_{16}$	25	40
4	$\text{Co}_{68.15-x}\text{Fe}_{4.35}\text{Ni}_x\text{Si}_{12.5}\text{B}_{16}$	24	44
2	$\text{Fe}_{77.5}\text{Si}_{7.5}\text{B}_{15}$	23	40
4	$\text{Fe}_{77.5}\text{Si}_{7.5}\text{B}_{15}$	25	42
M2	$\text{Fe}_{77.5}\text{Si}_{7.5}\text{B}_{15}$	22	39
M4	$\text{Fe}_{77.5}\text{Si}_{7.5}\text{B}_{15}$	23	44
M5	$\text{Fe}_{77.5}\text{Si}_{7.5}\text{B}_{15}$	23	43
M6	$\text{Fe}_{77.5}\text{Si}_{7.5}\text{B}_{15}$	23	44
M8	$\text{Fe}_{77.5}\text{Si}_{7.5}\text{B}_{15}$	23	44

1. Sample preparation

To test the core of the GCAF the glass coating was removed (G-R). The glass coating can be removed by either an acid etch of Hydrogen Fluoride (HF) or by

immersing the fibers in Liquid nitrogen. Glass removal by HF was done by immersing the sample fiber into a 50 volume percent solution of HF for 2 min. Glass removal by HF was used in all testing unless otherwise noted.

B. Analysis

1. Tensile testing

Tensile testing was measured using the apparatus shown in figure 2. The load cell has an input voltage of 12V and an output voltage in the -5 to 5 mV range. A 10mV to 5V analog amplifier was used to increase the load cell voltage so it could be measured by data capture software. A variable speed motor was used to raise and lower the bottom arm of the apparatus at 0.2mm/sec. Single fibers were tested using the sample preparation described in ASTM standard D3379-75.²⁰ The load cell was calibrated using hanging weights before measurements took place. The sample holder shown in Figure 3 was based on the ASTM standard.

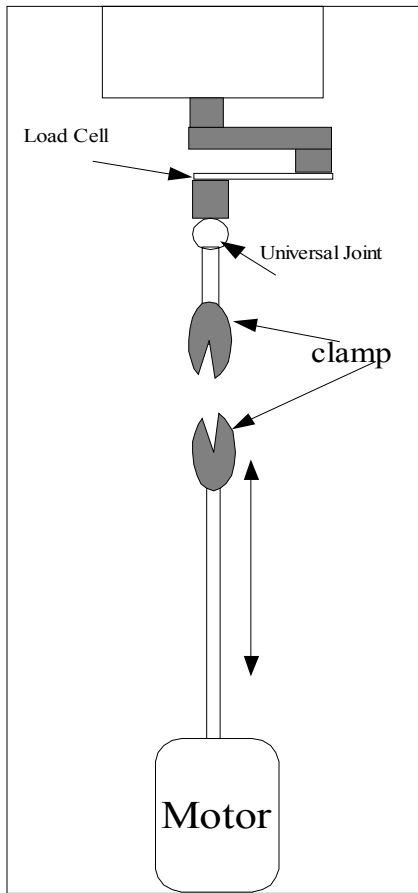


Figure 2. Fiber tensile tester.

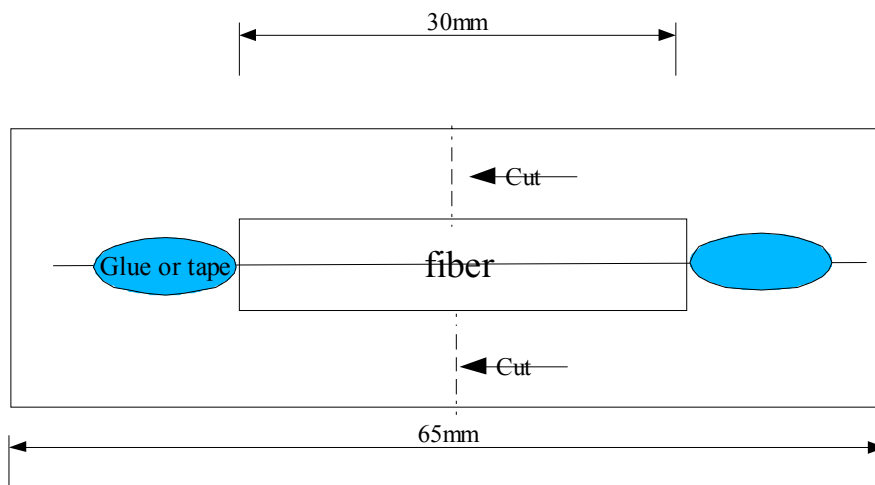


Figure 3. Fiber sample holder for tensile testing.

2. Elastic modulus analysis

The elastic modulus of the fibers was tested using a technique described by Daniel.²¹ A schematic of the testing apparatus is shown in figure 4. A length of fiber is placed horizontally on a rigid background. The deflection of the fiber as different weights are added is measured. The deflection of the fiber was measured using a traveling microscope that measured to one thousands of a millimeter. Using formulas 15 and 16 the stress and strain of the fibers can be calculated from weight and deflection. The elastic modulus can be calculated from the ratio of stress and strain. The accuracy of the device was tested using a borosilicate glass fiber. The fiber was found to have an Elastic modulus of 69 ± 5 GPa compared to a literature value of 72 GPa.²²

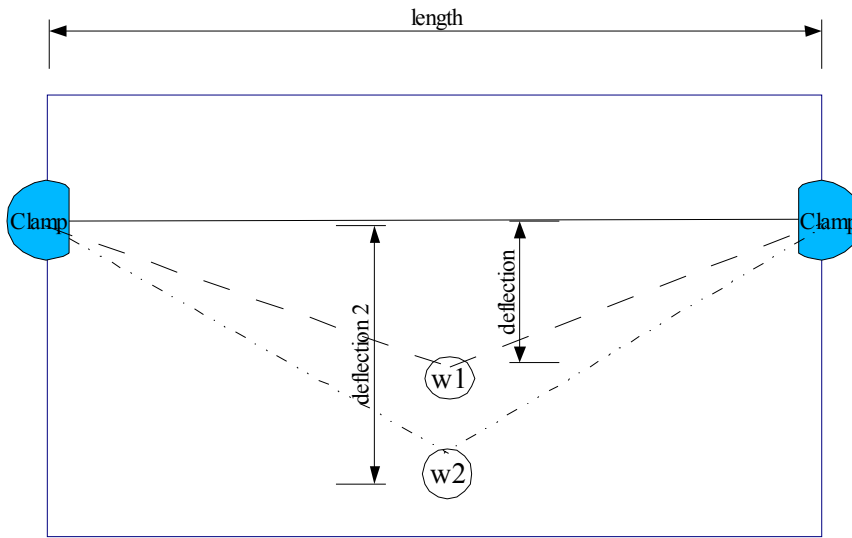


Figure 4. Device for modulus testing.

$$\varepsilon = \sqrt{1 + (2\delta_i / l)^2} - 1 \quad (15)$$

$$\sigma = \frac{W_i}{2A} \sqrt{(l / 2\delta_i)^2 + 1} \quad (16)$$

Where ε is the strain, σ is the stress, W_i is weight, δ_i is measured deflection of fiber, and l is the initial length of fiber.

3. Optical microscopy

Optical microscopy was performed on samples taped to the same sample holder as used for tensile measurements or taped to glass slides. Pictures were taken with a Polaroid digital camera connected to an Olympus BH-2 optical microscope with a polarizer. Video samples were collected using a NEC TI-26A black and white solid state video camera connected to a personal computer.

4. SEM

Samples were prepared for scanning electron microscopy (SEM) by mounting the fibers using conductive tape. SEM images were taken on an AMRAY SEM.

C. Magnetic sensor

The sensor device is shown in figure 6. The coil structure in this device is similar to devices constructed by Hison to measure the magnetostrictive properties of a silicone sheathed amorphous ribbon.²³ The device is similar in function to a transformer where the core material can be changed. In this case the core materials will be the GCAF. The sensor is driven by an alternating current source in the form of a signal generator. The inner coil acts as the transmitting coil and the outer coil acts as a receiver. The device can record the total output voltage and the output voltage of any harmonic oscillations produced by the GCAF using a signal analyzer sweeping from 10-200 kHz. The output waveform is also observed using an oscilloscope attached to the output. The sensors main capacity is observing the change in permeability of the core material. The output voltage of the sensor is a direct relationship to the permeability of the material in the sensor. As the permeability increases, the magnetic field at the sensing coil increases which in turn increases the output voltage. Using an oscilloscope attached to the sensing coil each fiber can be shown to give off a distinctive wave form. Using a signal analyzer the harmonic's produced by the core material can be observed. Figure 5 is a graph showing how the magnetic field at the sensing coil is influenced by materials having different permeabilities. This figure was created using the FEMM program.

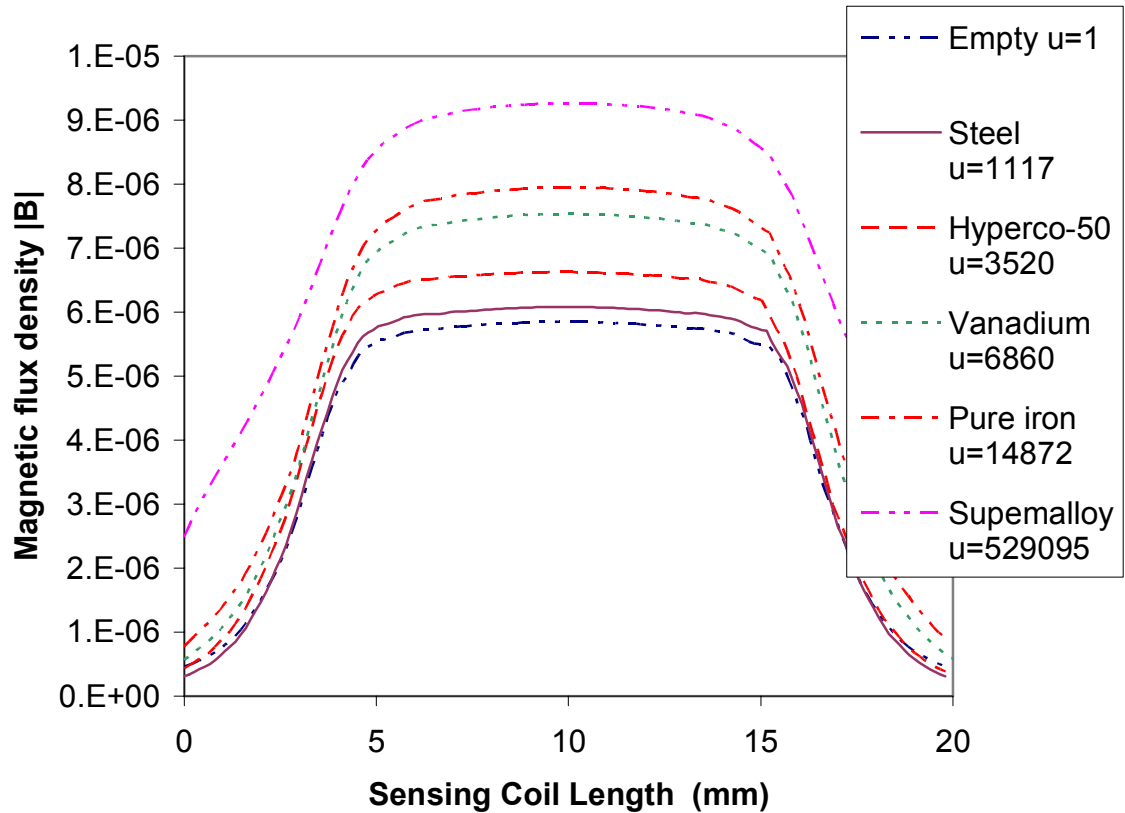


Figure 5. Change in magnetic field $|B|$ along the sensing coil as the permeability of the core material changes.

1. Construction

The sensing device (figure 6) is made from two copper solenoids in which one coil is larger than the other. The inner solenoid is the sensing solenoid has 28 turns and the outer solenoid is the driver has 46 turns. The other dimensions can be seen in the figure. The outer solenoid is driven by a function generator with an output of 173mA and 114.2mV at 19kHz. The output from the coil is measured with a signal analyzer (HP 3585 A) and an oscilloscope (Hitachi V-222).

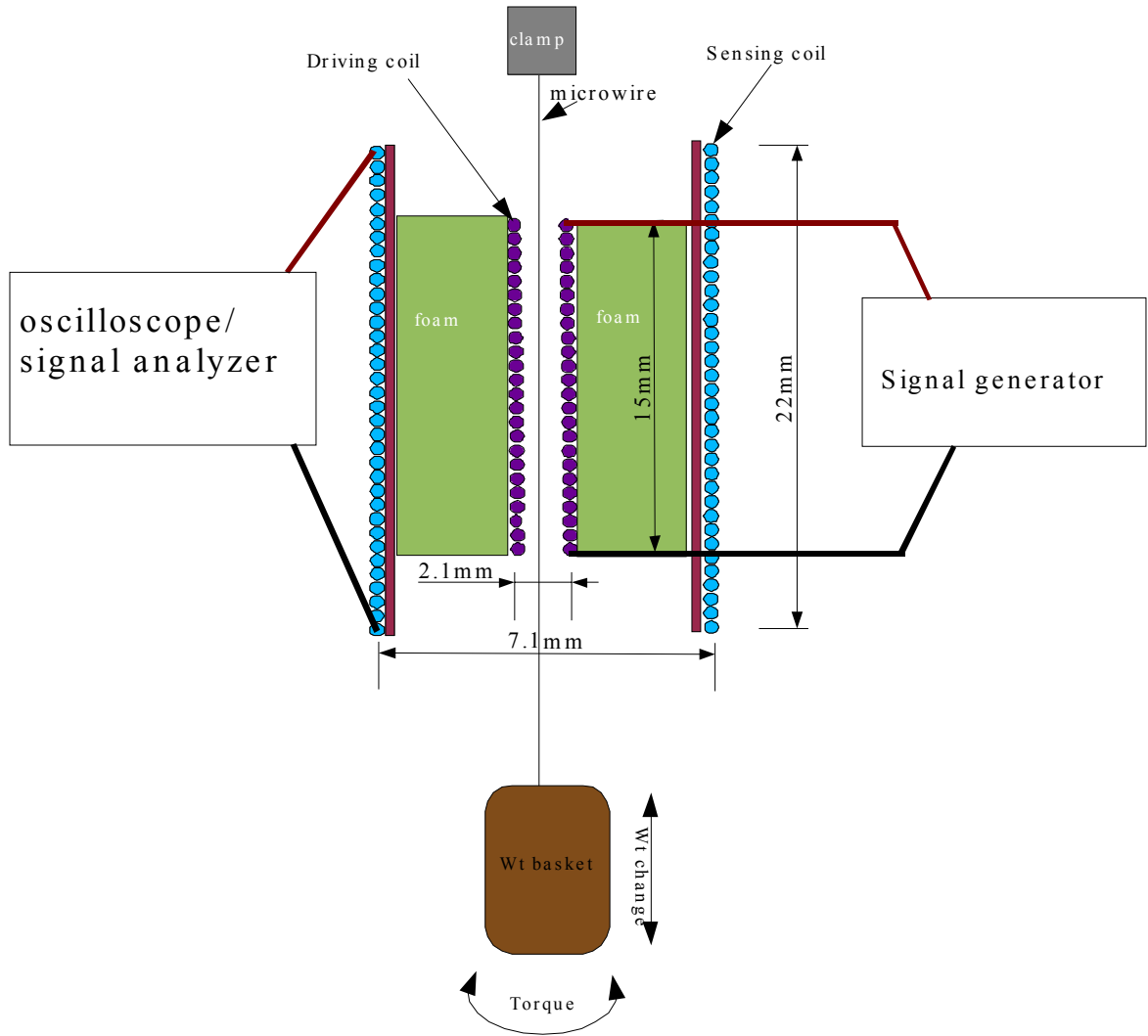


Figure 6. Sensor device.

2. Testing

The sensor was always tested empty before samples were added to take into account any day to day variations in magnitude or background noise. The GCAF were added by treading the fiber through the center coil. Unless otherwise noted GCAF samples were 3 times as long as the outer coil and centered with respect to the coil to reduce size effects and minimize testing variables. Fibers were tested as both as-received (A-R) and glass-removed (G-R).

a. Tension sensor

The sensor device can act like a load cell if the CoFeSiB or CoFeNiSiB fibers are used. The sensor was setup identical as per testing single fibers. A clamp was then added to the bottom of the fiber and incremental weights were added. The output voltages of the 1st through 9th harmonics were measured. The output was plotted against the force induced on the fiber by the weight and a calibration curve was created.

b. Torsion sensor

If the high Co based fibers were used the device could sense changes due to torsion forces on the fibers. The sensor setup is the same as for the tension sensor. However, a static weight on the fiber would be rotated clockwise or counterclockwise at 5 rotations per measurement and 7 measurements were taken in each direction. Output voltages were measured at each increment. The length of the fiber was noted at the beginning of each experiment so that torsion could be calculated.

3. Finite element analysis

A program called finite element magnetic method (FEMM) was used to model the sensor device in a finite element environment with respect to magnetic variables. The program is capable of modeling in two dimensions or axially.²⁴ The sensor device was modeled in an axial environment under the conditions of 19khz AC current going through the driving coil at 147 mA. The coil material was copper. When modeling GCAF as core material iron of a similar diameter was used in the FEMM. Figure 7 shows a screenshot of the FEMM modeled sensor under current with no core material.

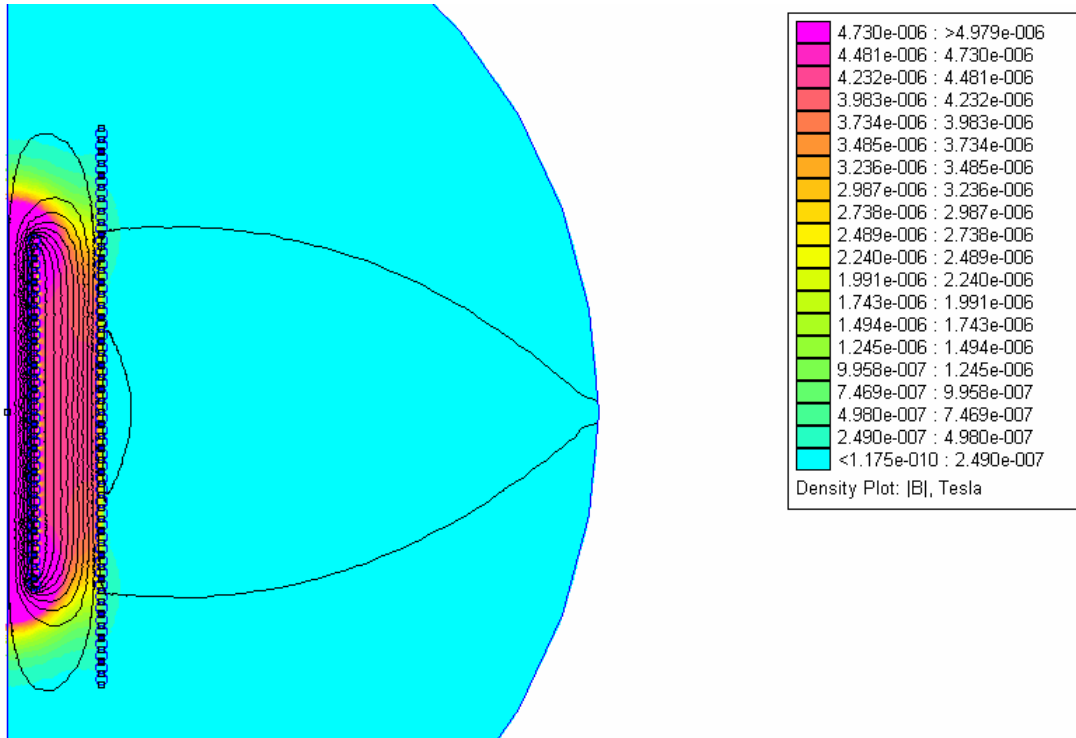


Figure 7. FEMM output showing magnetic flux lines and $|B|$.

III RESULTS AND DISCUSSION

A. Mechanical properties

1. Tensile

The true tensile properties are not easily calculated because of the way the GCAF behave. The fibers have a highly elastic core that can plastically deform as well as a brittle glass cladding. The breaking stress of the GCAF depends on the properties of the two materials, the bond between them, and the manner in which the materials fail when in contact with each other. Table 2 shows the tensile strengths of the GCAF tested. Values range from 800 to 1500 MPa. The majority of GCAF tensile strengths fall close to 1 GPa at their failing point.

Table II Tensile Strength of As-received Fibers

Designation	Composition	d _w μm	d _t μm	Tensile stress GPa	StDev GPa
2	CoFeSiB	24	40	1.077	0.009
3	CoFeSiB	23	38	1.554	0.025
4	CoFeSiB	25	39	1.285	0.025
M1	CoFeSiB	24	40	1.132	0.024
M4	CoFeSiB	25	40	1.152	0.044
4	CoFeNiSiB	24	44	1.092	0.153
2	FeSiB	23	40	1.155	0.018
4	FeSiB	25	42	0.812	0.054
M2	FeSiB	22	39	1.162	0.043
M4	FeSiB	23	44	0.933	0.018
M5	FeSiB	23	43	0.901	0.023
M6	FeSiB	23	44	1.129	0.044
M8	FeSiB	23	44	0.990	0.012
M7	FeSiB	25	36	1.295	0.032

When calculating breaking strength the diameter is assumed to be the outer diameter of the GCAF, i.e. the “Engineering Stress”. For fibers in which the glass coating fails first, the “true” maximum tensile stress is much higher. The fibers that show this behavior are the Cobalt based fibers and some of the nickel doped cobalt fibers. This makes comparing the breaking stress of the GCAF very difficult because if the glass coating fails the tensile properties depend on the tensile strength and diameter of the core only. Table 3 shows the breaking strength for some of the glass-removed samples.

Table III Tensile Stress of Glass-removed Fibers

Designation	Composition	dw μm	Tensile stress GPa	StDev GPa
2	CoFeSiB	24	2.936	0.032
3	CoFeSiB	23	4.263	0.058
4	CoFeSiB	25	3.024	0.035
M1	CoFeSiB	24	3.124	0.045
M4	CoFeSiB	25	3.162	0.025
4	CoFeNiSiB	24	3.316	0.043

It is interesting to note that when comparing the force at which the fibers break at there is no significant difference between the glass-covered fibers and the glass-removed fibers in the CoFeSiB system. This along with the fact that the glass cladding fractures before the ultimate tensile strength shows that the glass cladding has no positive or negative influences on the breaking strength of the core. The glass cladding does influence the apparent breaking stress by giving the fiber a larger diameter without increasing its properties.

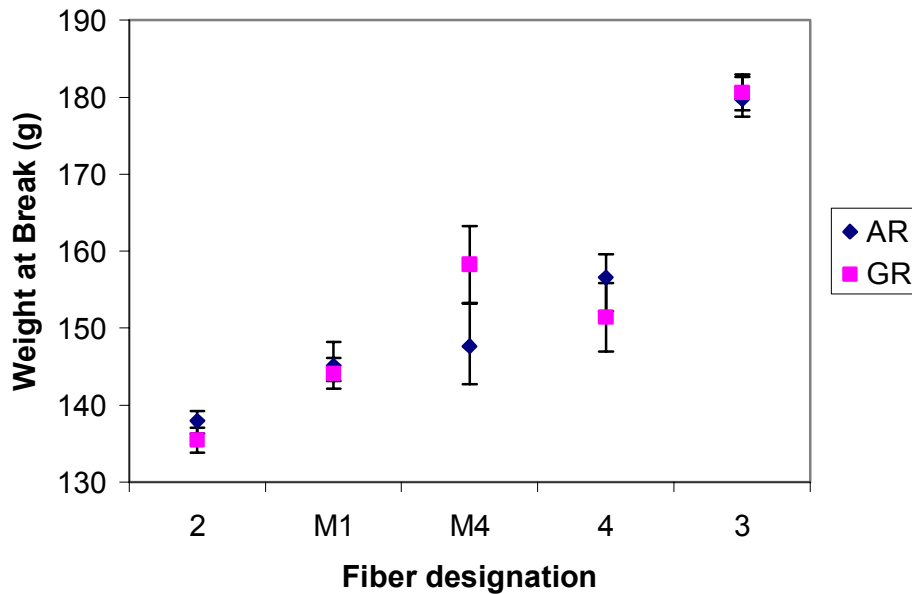


Figure 8. Comparison of the force at break between as-received and glass-removed CoFeSiB fibers.

2. Elastic modulus

The Elastic modulus of GCAF should follow the composite argument where the amount strain on the fiber is equally experienced by both the glass and the metal therefore the elastic modulus of the material will be a volumetric ratio of the two components and can be approximated by formula 1 assuming the glass to metal bonding is perfect. In reality the glass to metal bond is never “perfect” being that the two materials are intimately bonded at a mechanical and chemical level along the entire bond surface. Therefore, this formula should always overestimate the elastic modulus of the composite material.

Table 4 shows the elastic modulus for the different fiber compositions. All of the elastic moduli fall between 64 to 97 GPa. The elastic moduli of the G-R fibers are shown in table 5. The values for the G-R fibers vary greatly from 120GPa to 177GPa. There is a slight correlation between the observed elastic modulus and the diameter of the core, where the samples with the smallest diameters (23um) had a higher modulus than their counterparts.

Table IV Elastic Modulus of A-R Fibers

Designation	Composition	d _w μm	d _t μm	Elastic Modulus GPa ± 1
2	CoFeSiB	24	40	64.3
3	CoFeSiB	23	38	96.6
4	CoFeSiB	25	39	93.0
M1	CoFeSiB	24	40	69.4
M4	CoFeSiB	25	40	88.0
4	CoFeNiSiB	24	44	68.6
2	FeSiB	23	40	66.0
4	FeSiB	25	42	64.8
M2	FeSiB	22	39	65.9
M4	FeSiB	23	44	70.0
M5	FeSiB	23	43	65.3
M6	FeSiB	23	44	86.7
M8	FeSiB	23	44	89.8

Table V Elastic Modulus of G-R Fibers

Designation	Composition	dw μm	Glass Removed Elastic Modulus GPa
2	CoFeSiB	24	131±5
3	CoFeSiB	23	177±4
4	CoFeSiB	25	130±5
M1	CoFeSiB	24	121±5
M4	CoFeSiB	25	154±5
4	CoFeNiSiB	24	177±5
4	FeSiB	25	110±10
M4	FeSiB	23	175±5
M8	FeSiB	23	169±4

By using the Elastic modulus from the G-R samples and the modulus of a Pyrex type glass (approximately 67-68 GPa), it should be possible to predict the upper bounds of the composite Elastic modulus. Table 6 shows the estimated composite modulus using formula 1. The calculated modulus is higher than the experimental value for all of the samples except CoFeSiB 4. This result is curious because all of the other samples fit the model fairly well and the variation can most likely be attributed to either the bonding between the glass and metal or the condition of the glass coating on the tested GCAF (whether it is pristine or damaged).

Table VI Calculated Modulus Using Formula 1 Compared to Experimental

Designation	Composition	d_w (μm)	d_t (μm)	E_{comp} (GPa)	E_{comp} (GPa)	Difference (Calc-Exp)
				Calculated	Experimental	
2	CoFeSiB	24	40	87.3	64.3	23.0
3	CoFeSiB	23	38	104.6	96.6	8.0
4	CoFeSiB	25	39	90.4	93.0	-2.6
M1	CoFeSiB	24	40	83.7	69.4	14.3
M4	CoFeSiB	25	40	98.4	88.0	10.4
4	CoFeNiSiB	24	44	96.9	68.6	28.3
4	FeSiB	25	42	79.5	64.8	14.7
M4	FeSiB	23	44	93.4	70.0	23.4
M8	FeSiB	23	44	91.8	89.8	2.0

3. Mode of failure

The way the GCAF fail depends on the metal composition as well as the thickness of the glass coating. From empirical observation three distinct failure mechanisms occur. 1. As the fiber is elongated the stress is carried by both the core and the cladding until at both the glass and the metal fail at the same point (this behavior is seen in FeSiB and some CoFeNiSiB samples). 2. As the fiber is elongated the glass coating starts to crack circumferentially along the fiber. The force is not transferred directly to the spot of the first crack but instead more cracks start to propagate circumferentially along the length of the fiber, the cracks proliferate until one point in the metal core fails under the stress (this behavior is seen in CoFeSiB compositions). 3. The GCAF is elongated and behaves exactly like behavior 1 until the glass cladding rapidly fractures away from a central point along the length of the fiber. The measured load on the fiber is temporarily relieved, from the sudden elongation of the core. After the glass fractures the metal core is stressed until failure. This failure as well as the catastrophic failure is seen in CoFeNiSiB samples.

SEM and optical pictures of the fractured fibers looked very similar for all compositions. The metallic core did not show elongation at the fracture origin, and the failure point was smooth, as seen in figure 9, not elongated like creep failure. The glass cladding almost always fractured clean away from the metal core (figure10) showing that the glass to metal bonding was weaker than the intrinsic strength of the metal or glass. As seen in figure 11, glass did occasionally fracture while small pieces remained bonded to the metal indicating a strong bond between the glass and the metal in some places.

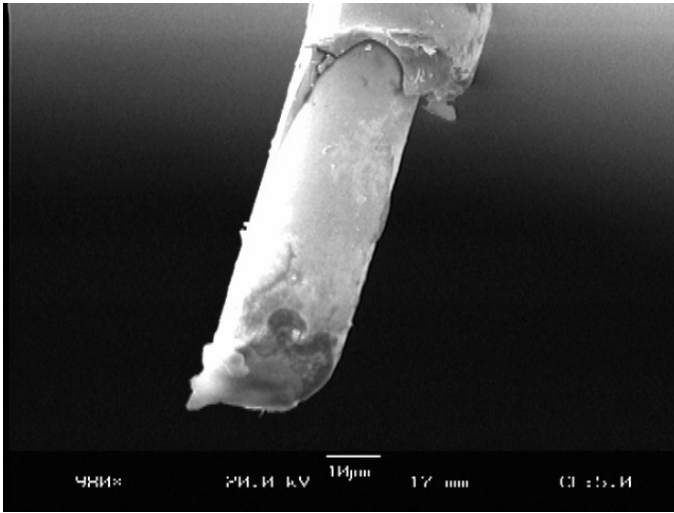


Figure 9. Fracture end of a FeSiB GCAF at 980x magnification.

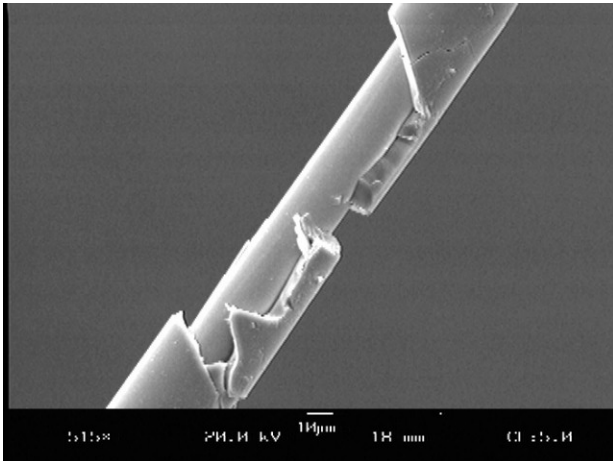


Figure 10. Glass fracture from core after tensile failure FeSiB GCAF.

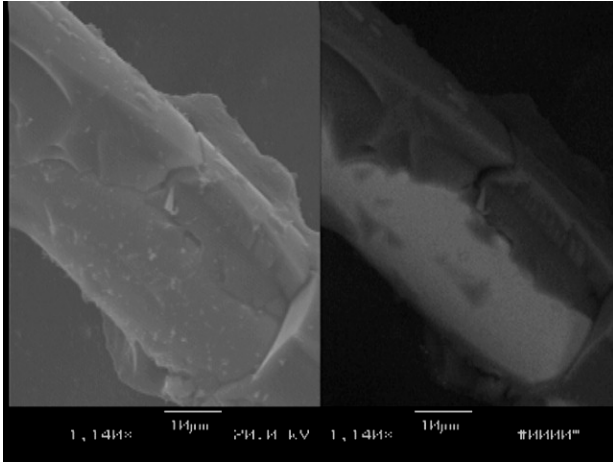


Figure 11. Glass fracture for CoFeNiSiB back scattered electron image dark regions represent glass.

a. CoFeSiB

The Stress strain curve for CoFeSiB compositions does not show artifacts of the glass cracking as are seen in the CoFeNiSiB samples. The curve is essentially linear and cannot be differentiated from the glass-removed samples. Figure 12 shows a typical stress strain curve for a CoFeSiB fiber. It is of note that the calculated elastic modulus using the stress strain curve is much lower than that calculated by Daniels method. This discrepancy is due to the fibers slipping during testing, leading to larger strain values being recorded than are actually experienced by the fiber.

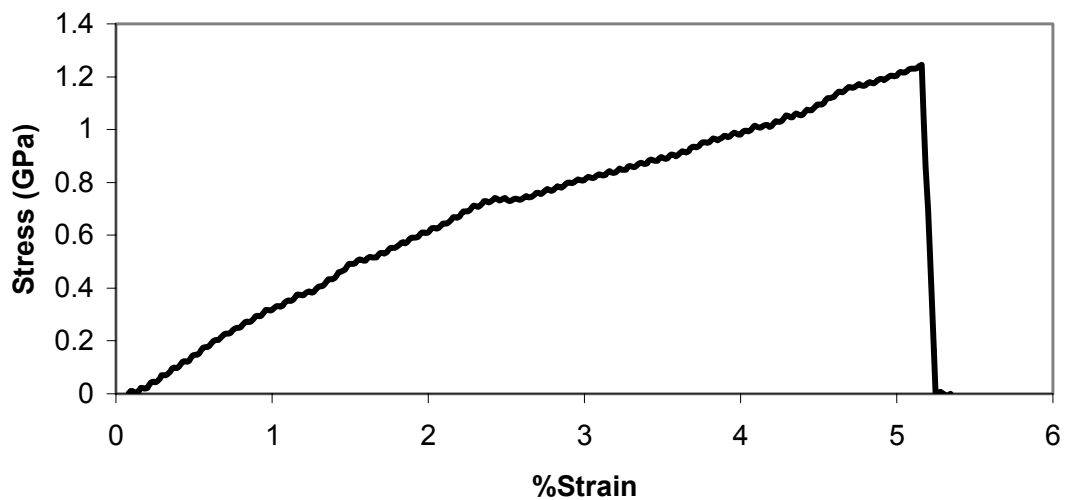


Figure 12. Stress strain curve for CoFeSiB 4.

The failure of CoFeSiB glass coating can be seen in figure 13. This shows frames from a video clip of CoFeSiB being fractured under tensile load. The progression of the cracking is fairly slow and the time between the first crack and the final breaking of the fiber is 6.75 seconds. The cracking of the glass may not extend all the way to the metal surface. The cracks may be blunted by the compressive stress in the glass. The blunting of the cracks can explain why the metal core does not fracture at the point of initial glass cracking and more cracks along the length of the fiber occur. This also indicates good bonding between the glass and metal creating the high compressive stress.

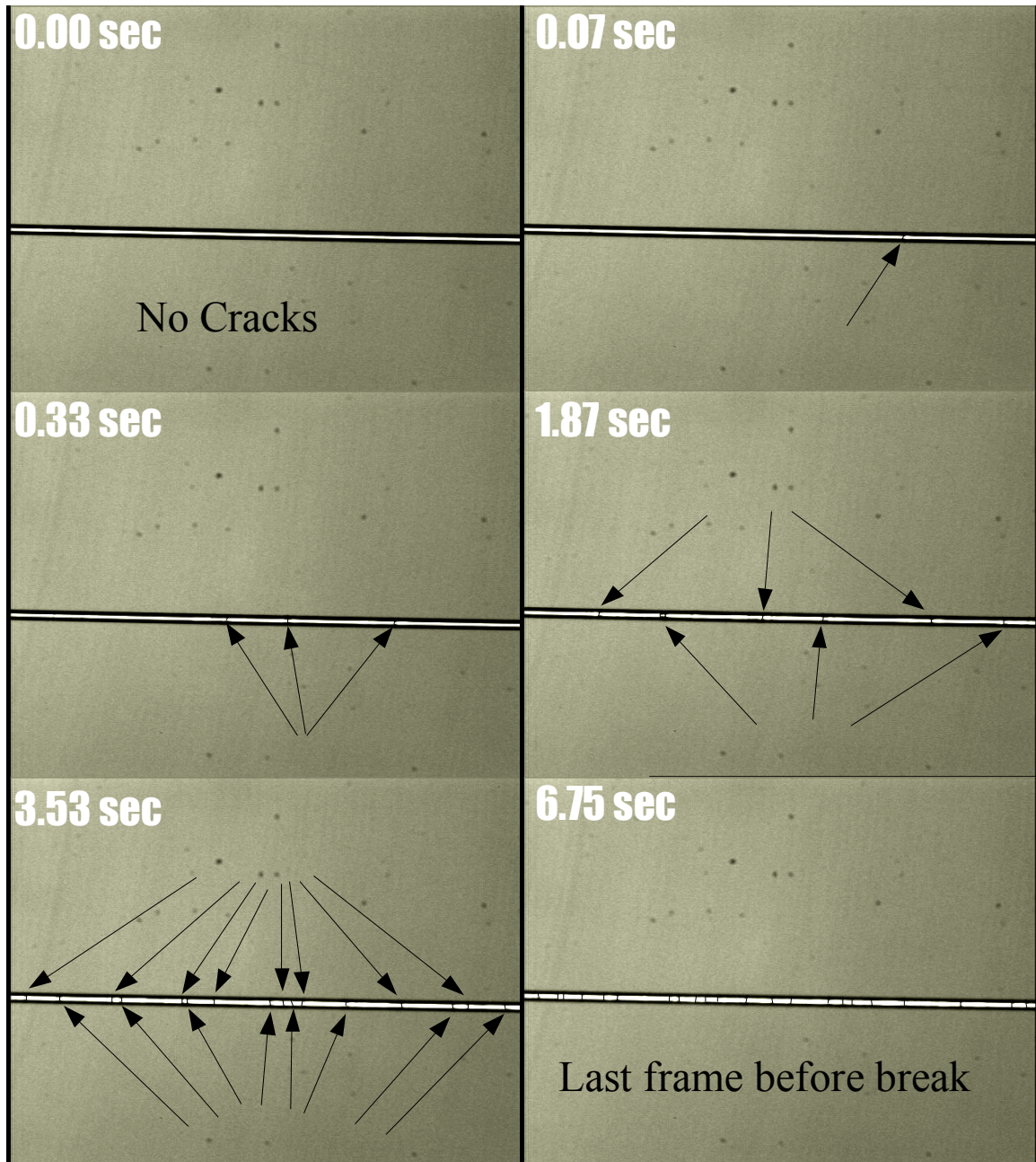


Figure 13. Video Frames of CoFeSiB cracking under tensile load.

b. CoFeNiSiB

Part of the CoFeNiSiB failure mechanism can be seen in its stress strain plots where there is a discontinuity in the slope. CoFeNiSiB fiber fails one of two ways as explained above. Figure 14 shows the stress strain plot of a fiber where the glass coating fails first. The sample continues to be loaded and the metal fails afterwards. Fibers that fail this way tend to have a lower tensile strength. The glass fails between 700 and 850

MPa in fibers that show the fast glass fracture behavior. Fast glass fracture fibers have an ultimate tensile strength just over 1 GPa with a low standard deviation. Figure 15 shows the stress strain curve of a CoFeNiSiB fiber that fails catastrophically having the glass fail at the same time as the metal. Fibers that fail this way tend to be the minority (1:6) but have on average a higher tensile strength than fibers failing the other way. Fibers that fail catastrophically always fail above 1 GPa and up to 1.35 GPa. However, the standard deviation is quite large.

The hypothesis for why the catastrophic failure method leads to higher stress is that the GCAF forming method places the glass in compression and the CoFeNiSiB fibers have a high glass to metal volume. Pristine glass coatings will resist cracking due to the compression and lead to a failure strength that is higher than the metal core would give alone. The GCAF are not assumed to have a pristine coating. However, some samples may have uncritical flaws and behave similar to a pristine fiber. In order to experience the compression needed to blunt cracks the glass metal interface must be strong. Furthermore, since each fiber has a different number and severity of flaws the standard deviation is much higher.

Figure 16 shows individual frames from a movie taken of a CoFeNiSiB fiber while undergoing tensile failure. The video shows the fast fracture of the CoFeNiSiB composition. Total time for fracture is just over 0.3 seconds. The video only shows about 1/3 of the fiber, and so the total fracture of the whole fiber would be longer approaching one second propagating away from the initial crack. This is much different compared to the CoFeSiB where glass fracture is very slow over the whole of the fiber. The time between the initial crack and the fiber finally breaking is 6.24 seconds which is about the same as the CoFeSiB fibers. Video was also taken of CoFeNiSiB in catastrophic failure. However, pictures do not show anything of interest because the camera is too slow to capture the failure.

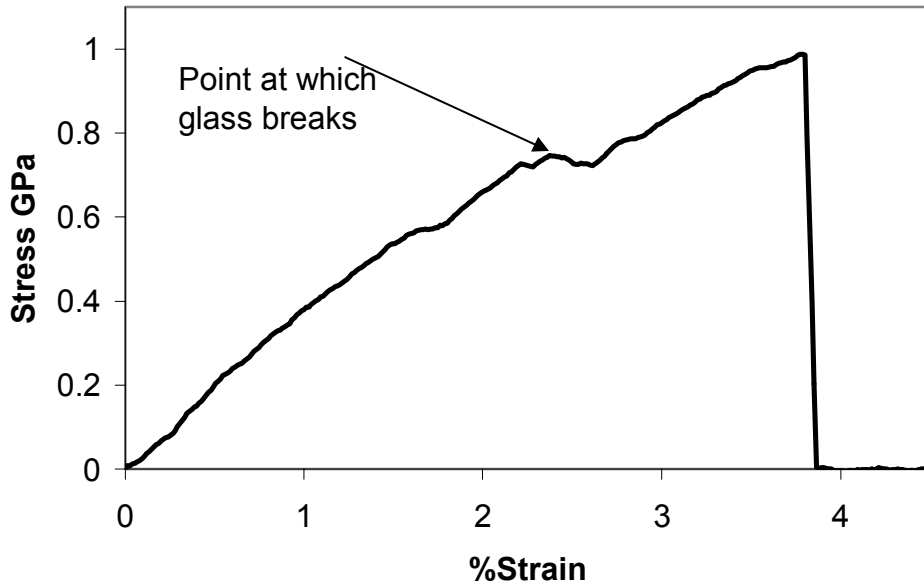


Figure 14. Stress strain curve showing CoFeNiSiB where the glass cladding fails.

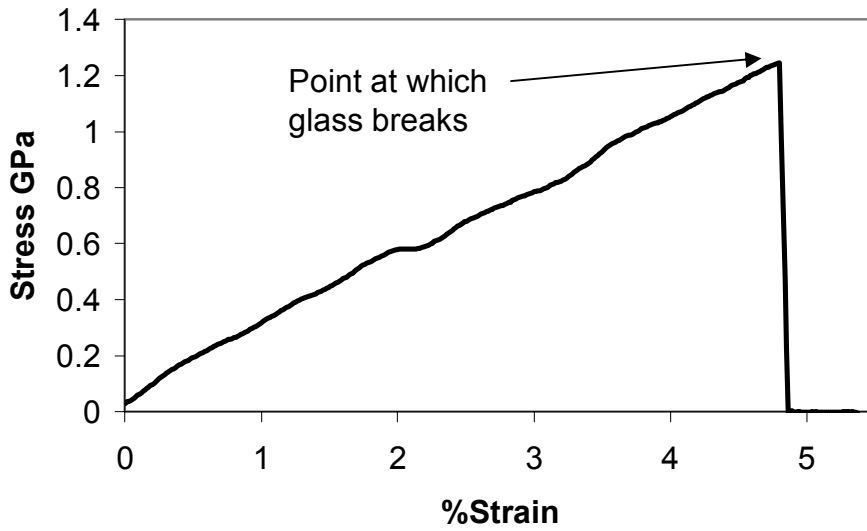


Figure 15. Stress strain curve showing CoFeNiSiB where the glass cladding fails when the fiber fails.

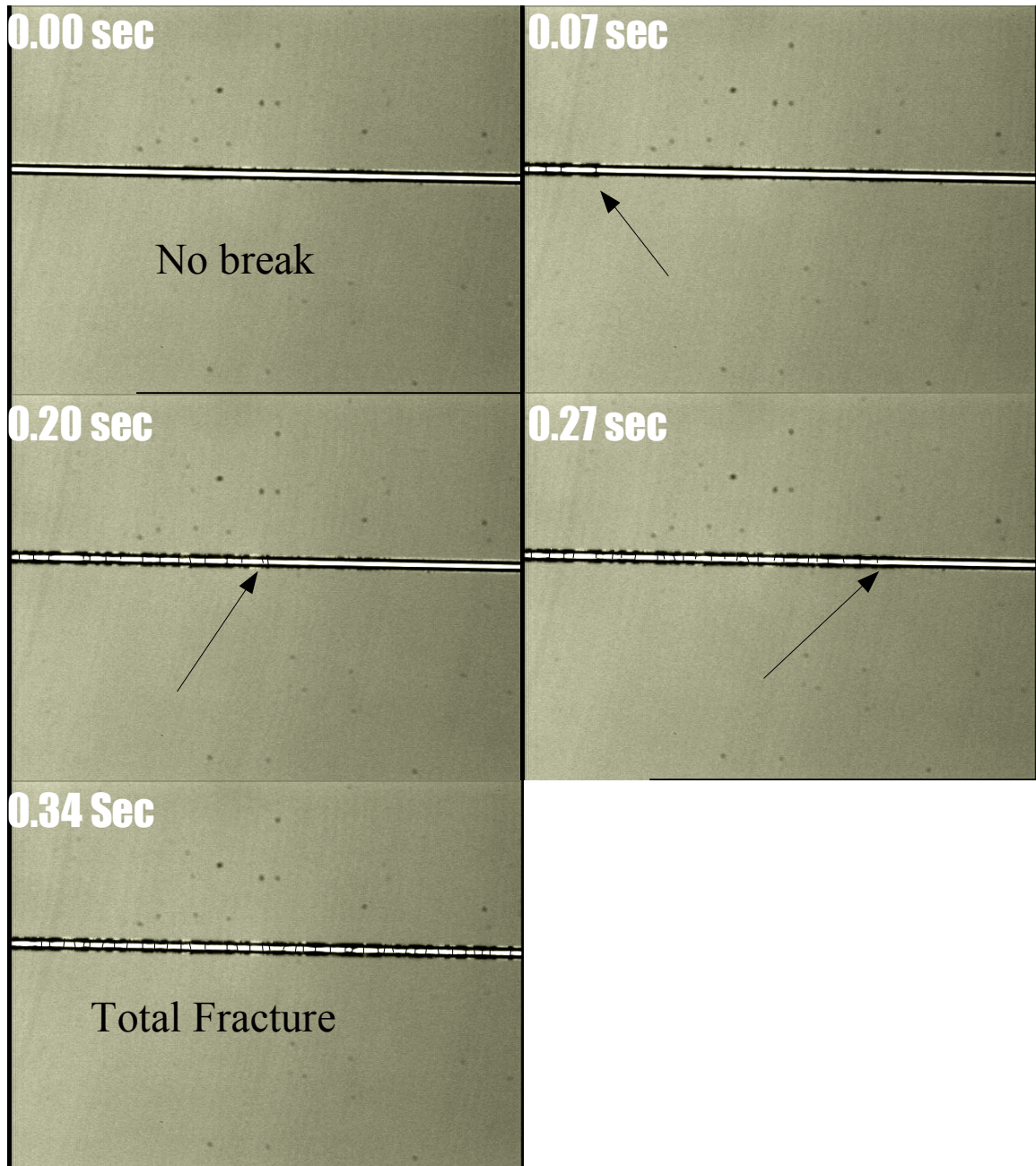


Figure 16. Video frames of CoFeNiSiB breaking under tensile load (arrow shows fracture progression).

c. FeSiB

A video of the FeSiB composition was also taken under tensile load to failure. The video does not show any cracking of the glass coating until the failure of the entire composite fiber (catastrophic failure). After the GCAF has fractured the coating is observed to be cracked and chipped similar to the other compositions after fracture. The

stress strain curve for the FeSiB specimens with thicker glass cladding look similar to the stress strain curve of CoFeNiSiB showing fast fracture. This is interesting because none of the samples videoed showed a fast fracture behavior. Figure 17 shows the stress strain curve of FeSiB M6 and the arrow designates the discontinuity that might be a fast glass fracture. The discontinuity occurs between 700 and 850 MPa for FeSiB M6 similar to the CoFeNiSiB composition. It is possible that fast glass fracture is a function of the strain rate. The strain rate taken for the videos was about half the strain rate used in tensile testing.

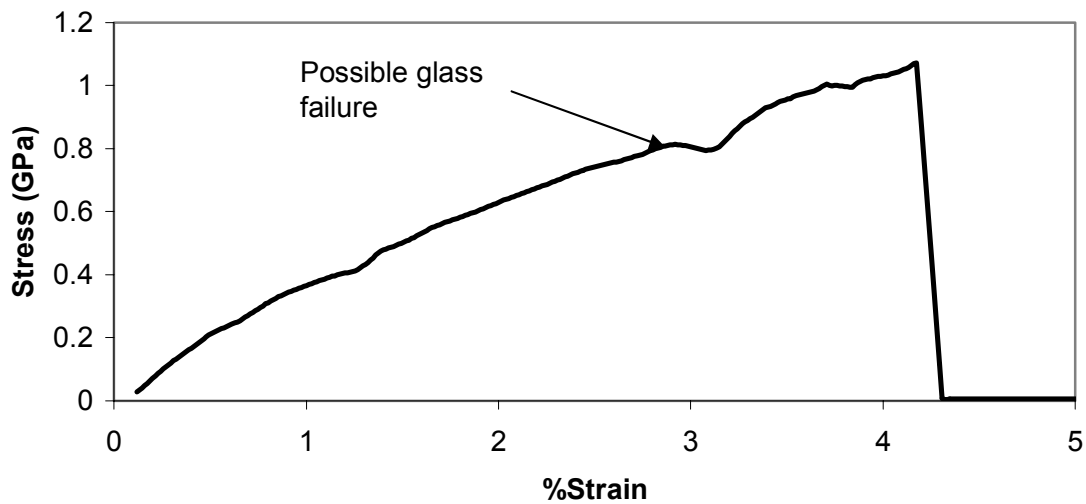


Figure 17. Stress strain Curve for FeSiB M6.

B. Heat treatments

Crystallization of the GCAF metal core can be achieved by heat treating the samples above 550°C. The crystallization starts almost immediately, and the extent and magnitude of the crystallization grow with increasing heat treatment time. Devitrification changes the failure characteristics of the GCAF core from an amorphous metal to that of a relatively brittle crystalline metal. The elastic modulus of crystalline metals is generally higher than that of amorphous metals. However, the effective tensile strength

of a crystalline metal is usually lower than that of the amorphous counterpart due to creep and dislocation motion.

Table 7 shows how crystallization changes the breaking strength of a fiber. The initial change in properties is dramatic. Further crystallization (longer times at temperature) does not seem to change the breaking strength by any significant value. During crystallization of the metal the glass coating should not be affected because of the short time allowing minimum relaxation to take place. The bonding between the metal and the glass might be changed by crystallization and should be further investigated. The change in the tensile strength of the core leads to the conclusion that fibers that have more glass area are not affected as much as their lower glass area counterparts. FeSiB M7 and CoFeSiB 4 have S values (Cladding area/Core area) of 1.07 and 1.43 respectively FeSiB M8 has an S value of 2.66, a value that is much higher than the two aforementioned samples and translates to a tensile strength that is less sensitive to devitrification of the core as seen in table 7.

Table VII Fiber Strength after Crystallization

Designation	Composition	Heat Treatment min @ 575C	Breaking Strength GPa	StDev GPa	% of original
4	CoFeSiB	0	1.067	0.146	100
4	CoFeSiB	5	0.690	0.123	64.6
M8	FeSiB	0	0.990	0.012	100
M8	FeSiB	5	0.889	0.053	89.7
M8	FeSiB	15	0.860	0.062	86.8
M7	FeSiB	0	1.295	0.032	100
M7	FeSiB	5	1.001	0.135	77.2

C. Magnetic properties

The magnetic properties of the GCAF were tested using the apparatus shown in figure 6. The permeability of the GCAF core as well as the harmonic oscillations produced by the GCAF core from the influence of the magnetic field were the basic magnetic properties measured with the device. Analysis of the test results concentrated

on relating the change in these harmonic oscillations and permeability to stress on the core from three sources: the stress induced in the core by the glass coating during manufacture, the stress on the core from a tensile load and the stress on the core from a torsion load. All three compositions were tested. However, the FeSiB composition did not respond as well in the sensor, and tension and torsion measurements were not possible. This is most likely due to the fact that the permeability of FeSiB composition is not as readily changed by stress and therefore less susceptible to being measured in the sensor.

1. Harmonics

a. FeSiB

Figure 18 shows the normalized harmonic for harmonics 2-13 for various FeSiB samples. The normalized harmonic is a way to minimize day to day variations from outside influences on the sensor output as well as making graphs easier to interpret because the primary harmonic is 10 times stronger than the others. The normalized harmonic is calculated by dividing the harmonic of interest by the primary harmonic and multiplying by 100. As seen in the chart not all of the fibers show the same pattern of harmonics. One FeSiB fiber designation (2) shows strong odd-numbered harmonics like the other two compositions (CoFeSiB and CoFeNiSiB). Several designations (M2, M6, M8, M5) show stronger even harmonics. Designation 4 shows both even and odd harmonics but neither is strong nor weak. Finally, designation M4 shows almost no harmonic output other than the primary.

Figure 19 shows the normalized harmonics of FeSiB fibers after the glass coating has been removed. It is much easier to see a trend in the harmonics from these samples. M2, M4, M5, M6 and 2 now all have stronger odd harmonics than even ones. M8 still shows a high 2nd harmonic but the remaining even and odd harmonics are approximately equivalent. FeSiB 4 still has almost no harmonic output other than the primary harmonic. Figure 20 compares the output voltages from the harmonics of two FeSiB compositions both of which were chosen because they showed opposite behavior and encompassed the entire spectrum for all the FeSiB fibers. The M2 designation has a decrease in harmonic intensity when the glass coating is removed while the M4 designation has an increase in

harmonic intensity when the glass coating is removed. The other compositions fall in-between these two extreme cases and designation 4 shows almost no change in harmonic output between A-R and G-R.

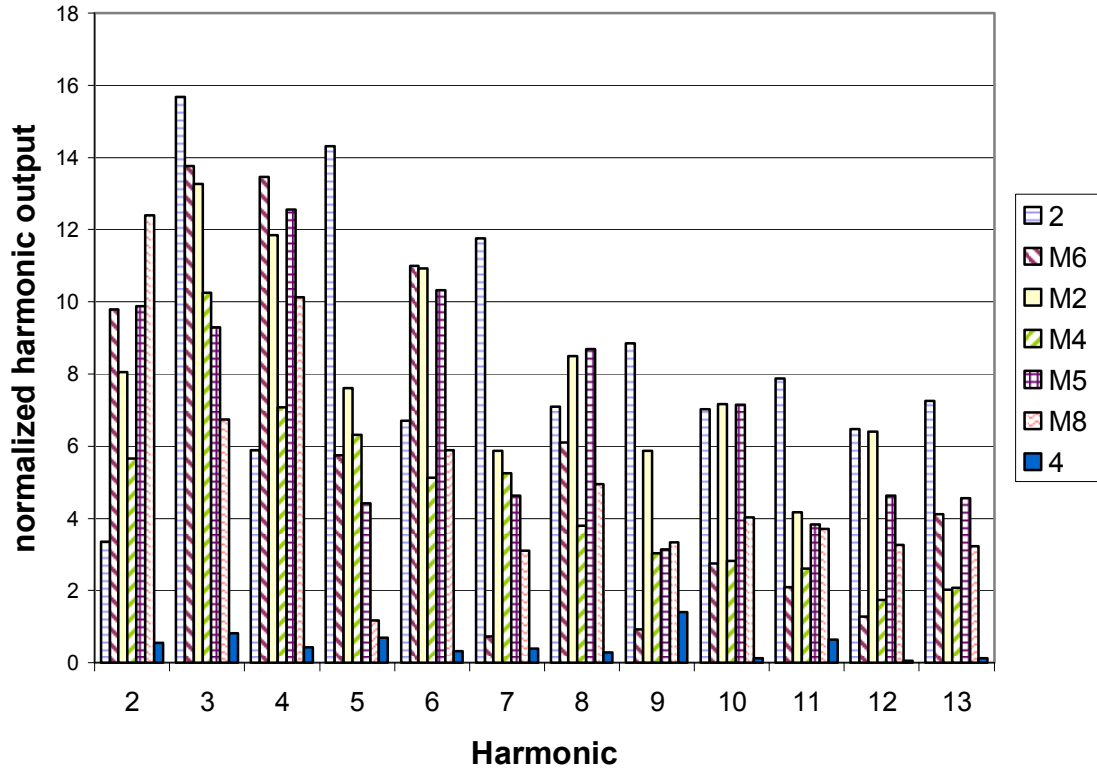


Figure 18. Harmonic components of FeSiB as-received fibers.

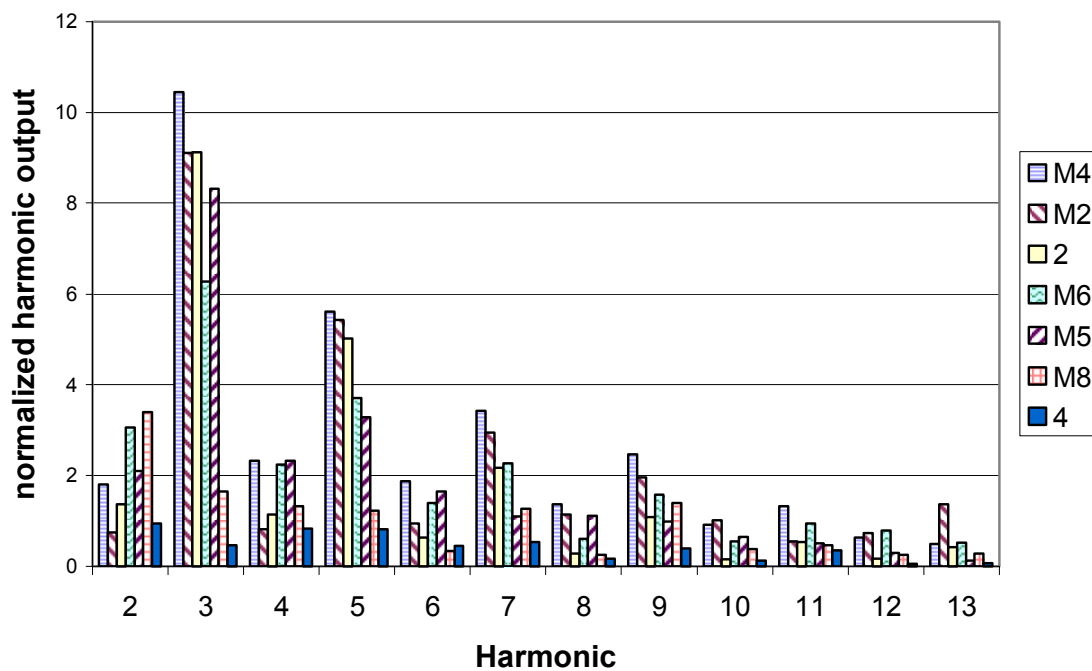


Figure 19. Percentage Harmonic components of FeSiB glass-removed fibers.

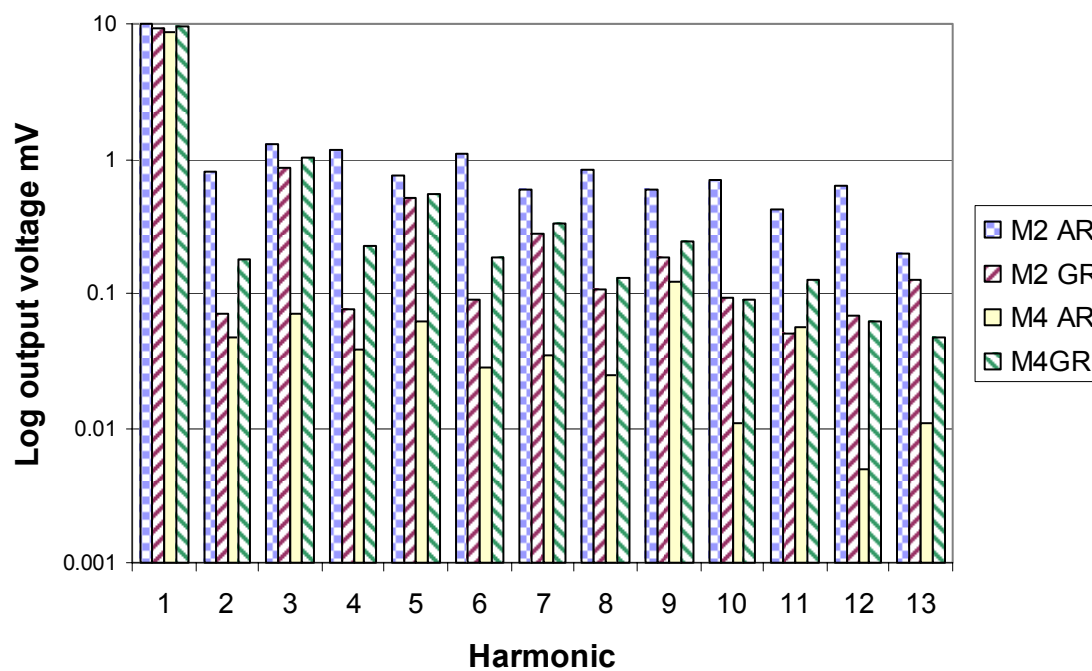


Figure 20. Comparison of as-received and glass-removed samples for FeSiB.

b. CoFeSiB

The harmonic components of the CoFeSiB GCAF are very regular compared to the irregularity of the FeSiB composition. All of the CoFeSiB designations show strong odd harmonics. The CoFeNiSiB composition also has strong odd harmonics and in most respects very similar to the CoFeSiB composition. Figure 18 shows the normalized harmonics for A-R CoFeSiB and CoFeNiSiB compositions. Figure 22 shows the normalized harmonics for CoFeSiB and CoFeNiSiB glass-removed samples. It is seen that the pattern of strong odd harmonics does not change with the removal of the glass and the relative strengths of the harmonics are preserved. The difference in the output of the harmonics between the A-R and G-R samples is a function of the stress that the glass coating places on the metal core. This is shown later in the section on mechanical and magnetic coupling. Figure 23 shows the change in the output voltage of the harmonics for a few CoFeSiB samples. All of the designations follow this trend of the G-R samples having higher outputs than the A-R samples.

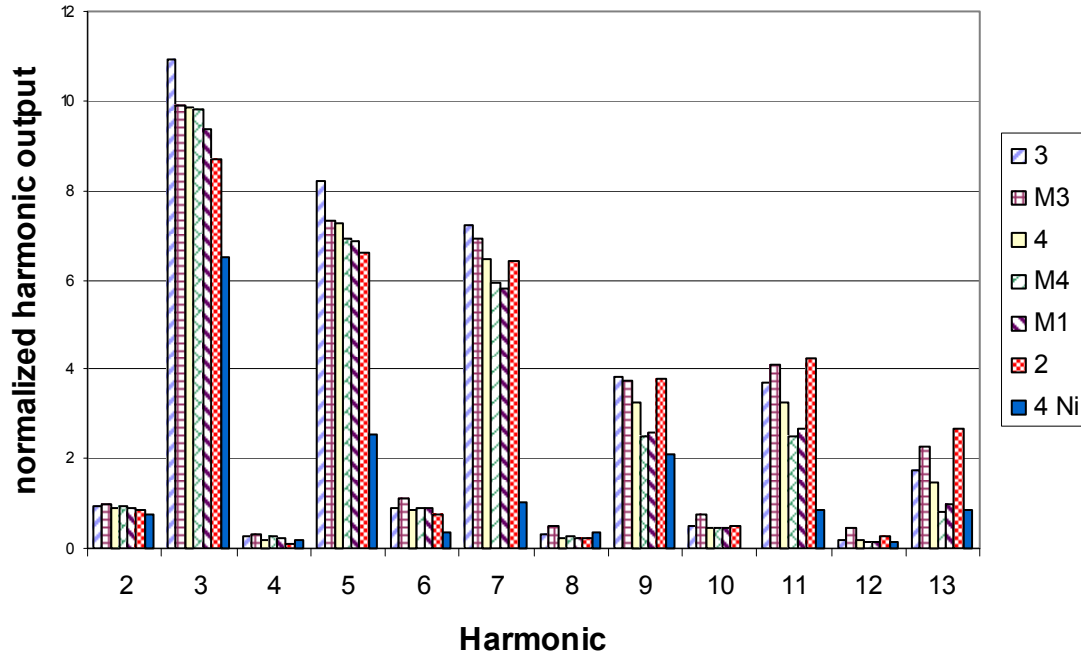


Figure 21. Harmonic components of CoFeSiB as-received fibers.

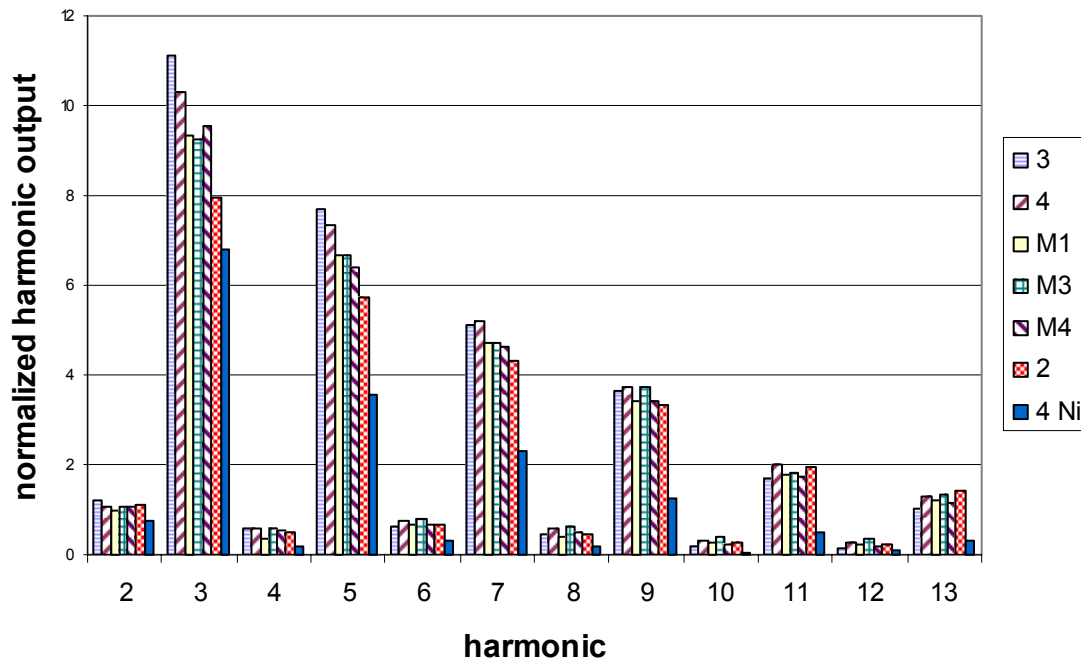


Figure 22. Harmonic components of CoFeSiB glass-removed fibers.

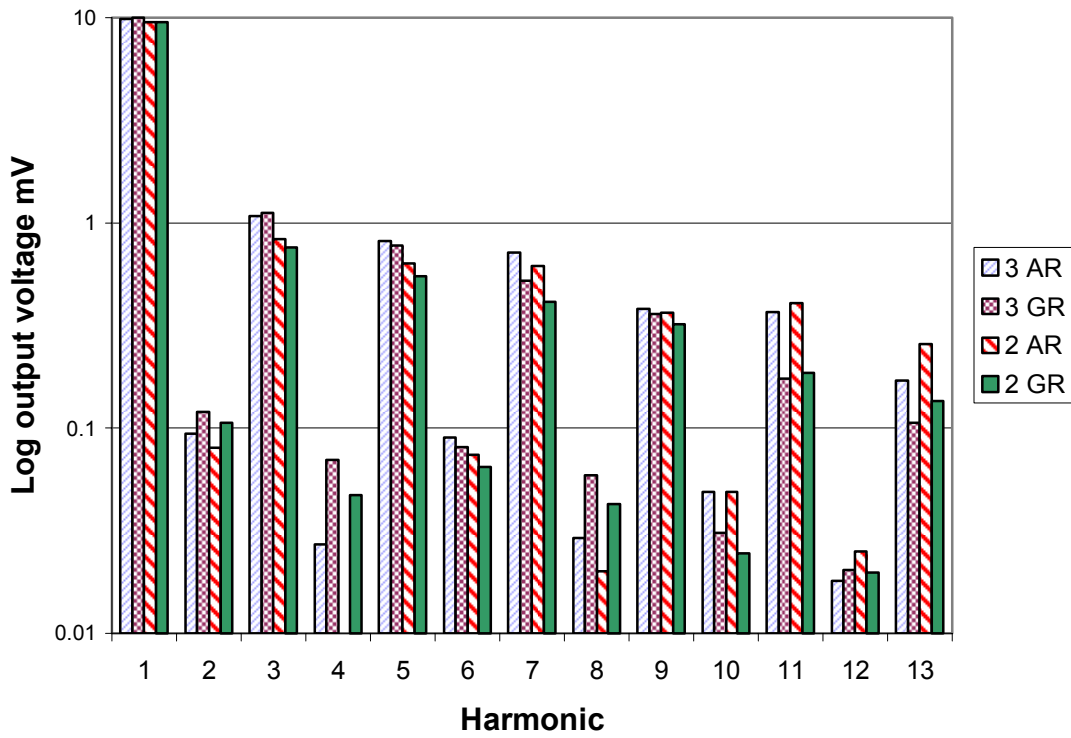


Figure 23. Comparison of as-received and glass-removed samples for CoFeSiB.

2. Waveform shapes (occiloscope)

The oscilloscope easily shows the combined effect of all harmonics and the differences between the different compositions opposed to the individual harmonic analysis of the signal analyzer. However, it is much more qualitative and all observations are empirical. The shape of the waveform easily distinguishes the FeSiB GCAF from the Co-rich samples.

a. FeSiB

Figure 24 shows a typical waveform for an A-R FeSiB composition it can be seen that the harmonics show up as the off centered spike to the right of the peak voltage. This spike is shifted towards the peak as seen in figure 25 when the glass coating is removed. The movement of the spike is a function of the stress produced by the glass.

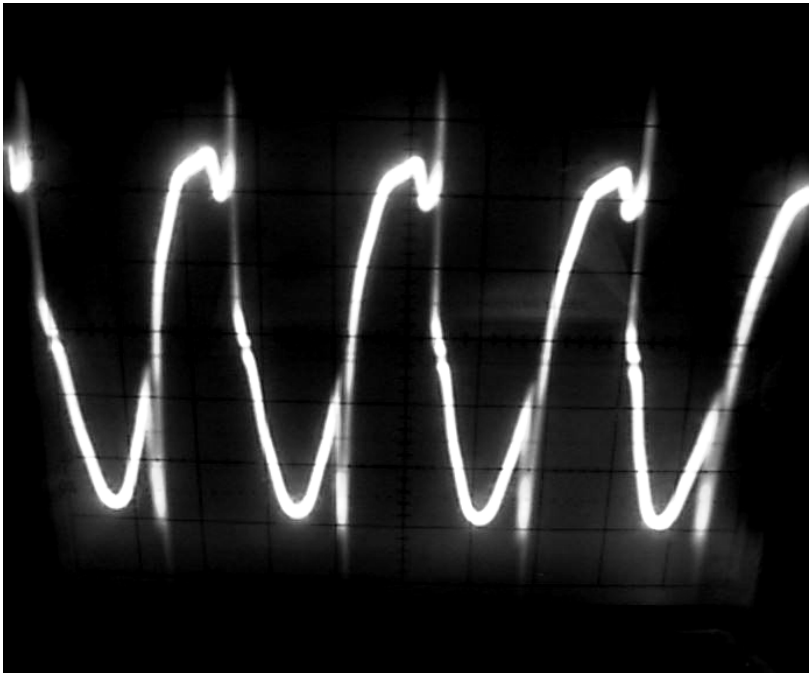


Figure 24. FeSiB M7 as received.

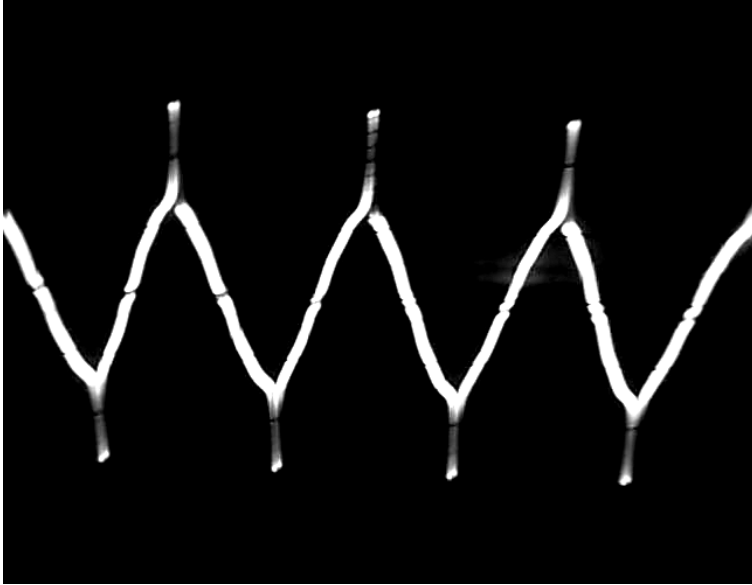


Figure 25. FeSiB M7 glass-removed.

b. CoFeSiB

The CoFeSiB and CoFeNiSiB waveforms are similar displaying a spike or hump at the peak voltage. The shape of the spike varies with the stress on the metal core. As more stress is placed on the core, the amplitude of the spike decreases and becomes more rounded. This provides a qualitative measure of the stress the glass coating places on the metal core. Figures 26, 27 and 28 show the waveforms produced by three different fibers, each of which exhibit a different intensity spike. It is seen that the spike of CoFeSiB M3 is larger than CoFeSiB 2 and that both of them are larger than CoFeNiSiB. The stress the glass places on the metal core using the formula given by Chiriac depending on the ratio of the glass cladding area to the core area follows the same trend. The stress on the metal calculated from formula 14 σ_{zz}^m is 272.7MPa for CoFeSiB M4, 299.1MPa for CoFeSiB 2, and 360.8 MPa for CoFeNiSiB 4.

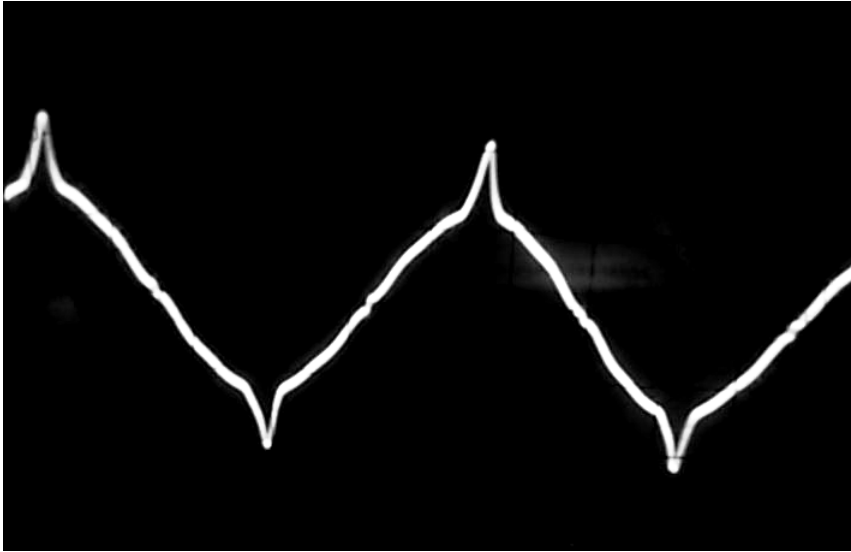


Figure 26. CoFeSiB M3 A-R.

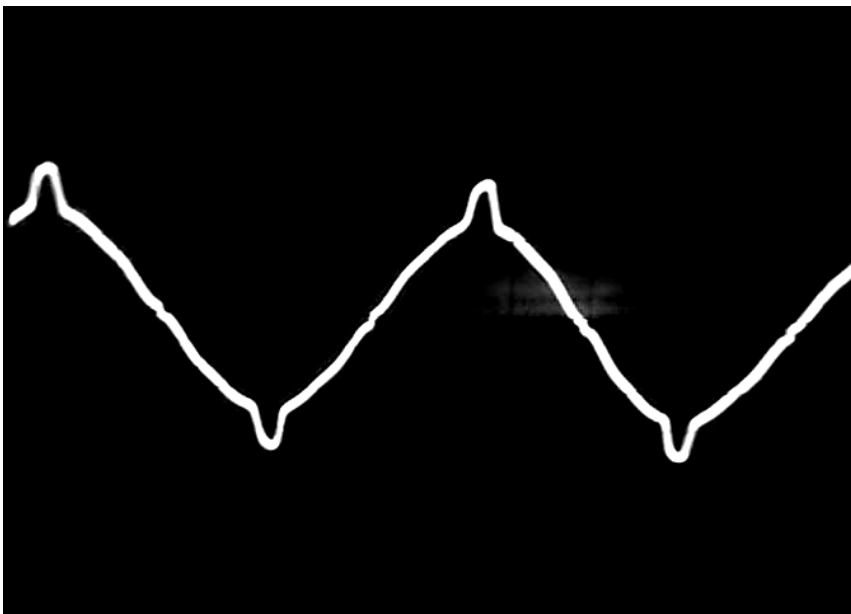


Figure 27. CoFeSiB 2 A-R fiber.

c. CoFeNiSiB

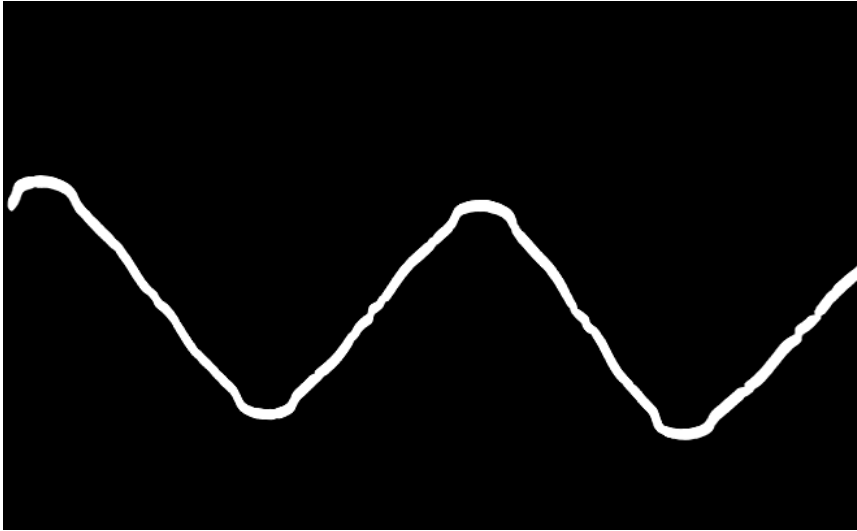


Figure 28. CoFeNiSiB 4, A-R .

3. Multiple fibers and fiber size

GCAF are being evaluated as identification tags as well as other sensors in which the fiber might also provide some benefit as a reinforcing component of the composite. With these applications in mind it is interesting to note how multiple fibers interact and how the volume of material in the sensor changes its output.

a. Multiple fibers

The spike is dependent on the number of fibers and therefore the volume of metal in the sensor at a given time. Figure 29 shows how the spike changes as multiple fibers are added into the sensing device. The magnitude of the spike is a function of how many fibers are added, but the sharpness of the peak stays the same. If two different GCAF are placed in the sensor, the spike height is additive and its sharpness is somewhere in-between the two individual samples. Figure 30 shows this behavior with CoFeSiB 2 and CoFeNiSiB 4.

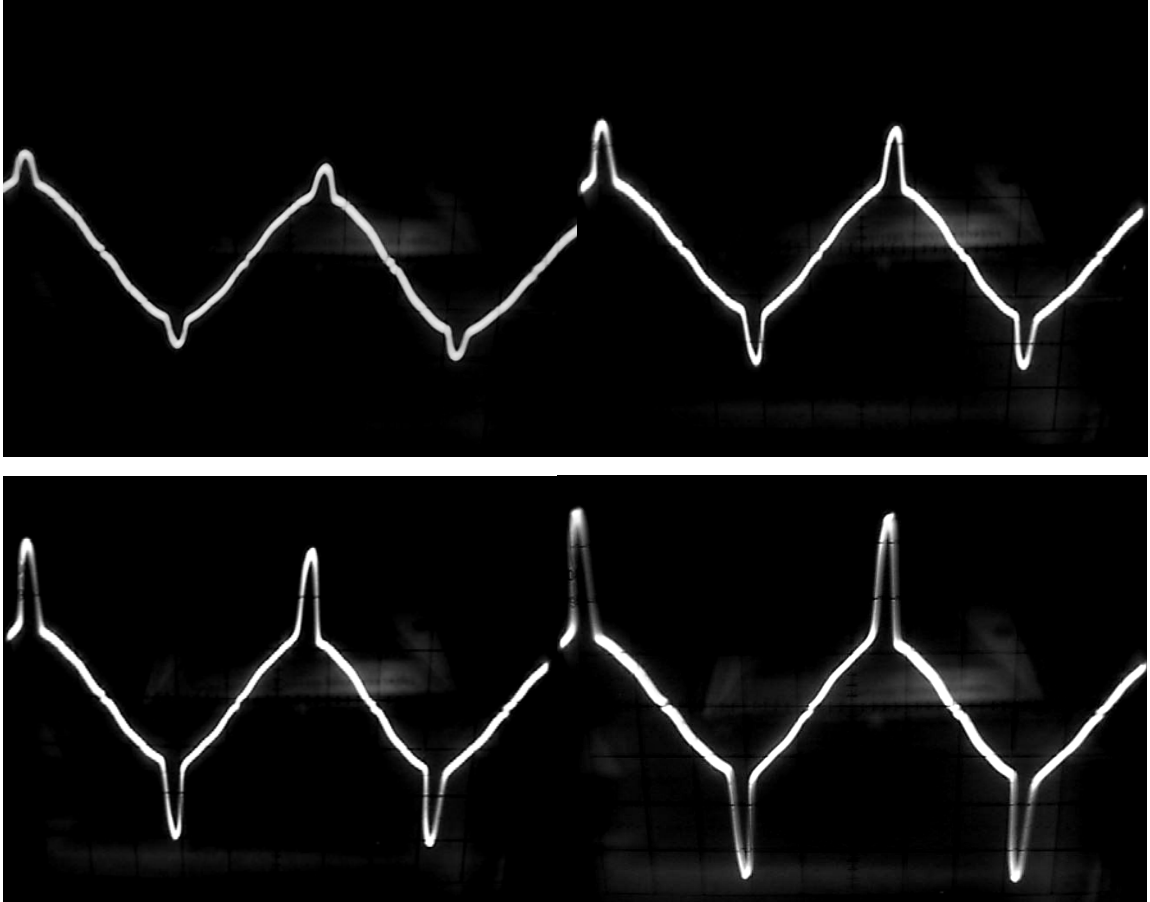


Figure 29. Oscilloscope readings for multiple fibers. The number of fibers progresses from 1 to 4 starting in the upper LH corner ending in the lower RH corner.

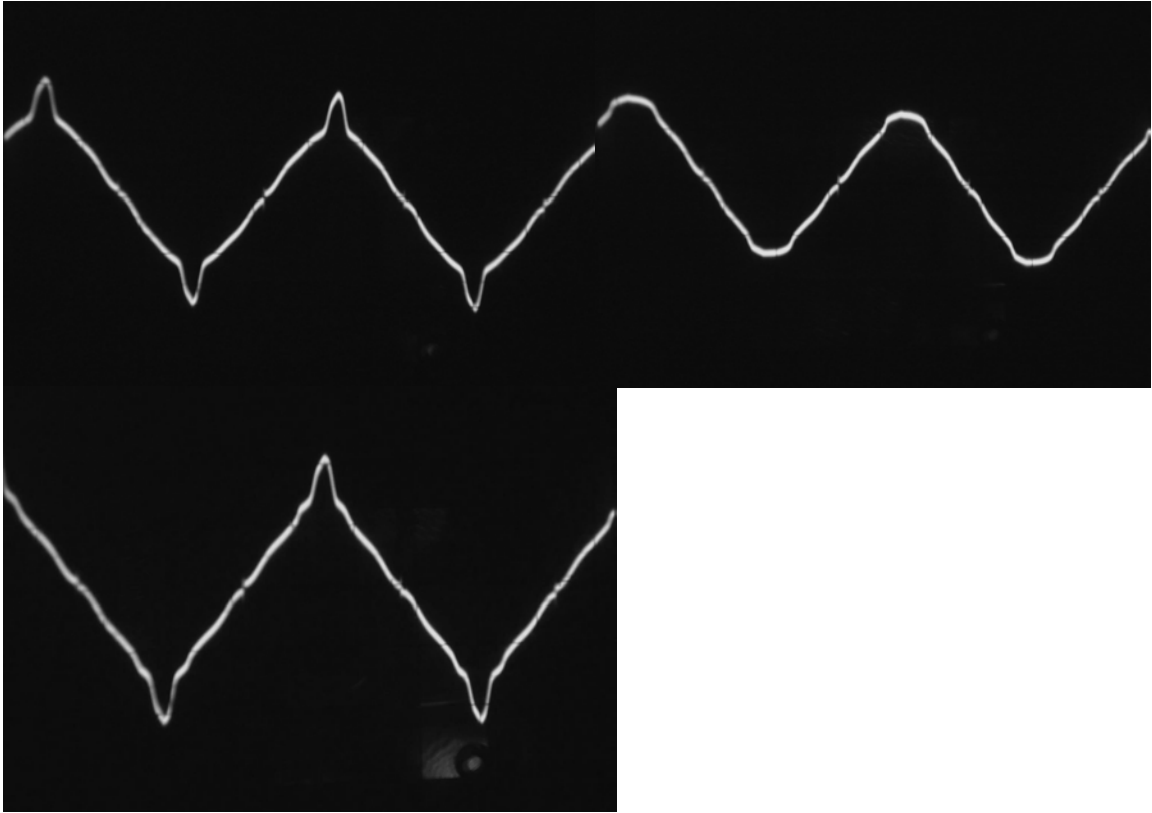


Figure 30. Upper LH side CoFeSiB 2 upper RH side CoFeNiSiB 4. Bottom both fibers in sensor showing combined signal.

Figures 31 and 32 show the effect of multiple fibers on the harmonic oscillations that are produced. Figure 31 shows the change in the outputs of both the even and odd harmonics as more fibers are added. However, the even harmonics are initially very low in this system such that their change is trivial compared to the odd harmonics. Figure 32 shows the slope of the different lines from Figure 31 comparing two different CoFeSiB designations. A comparison of the fibers shows that even though the designations behave similarly, they can still be differentiated in how the harmonic output scales with additive fibers. The percentage increase for each harmonic is the same it is just a factor of the initial output voltage, i.e. the output of 2 fibers is twice that of one fiber and the output of 3 fibers is three times that of a single fiber.

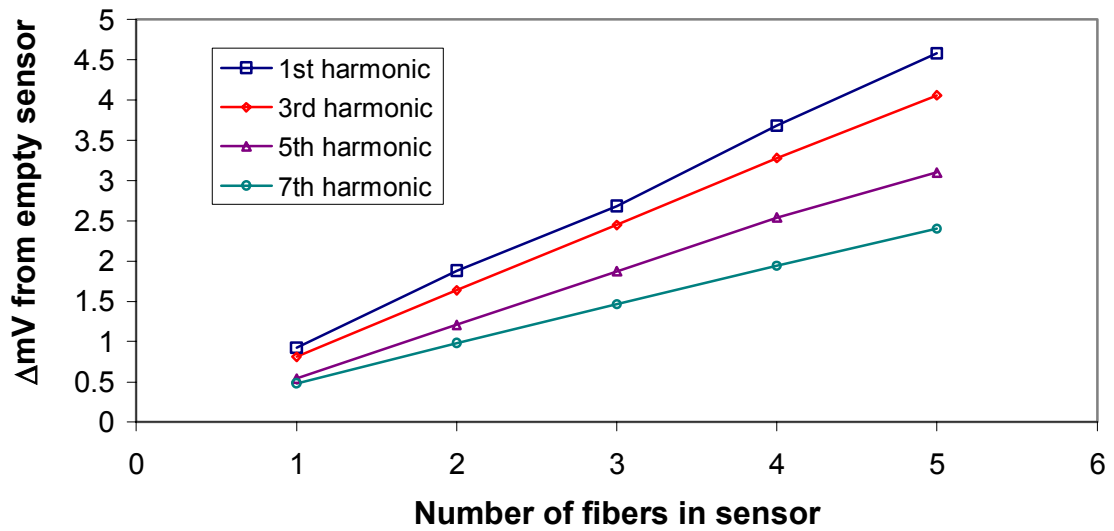


Figure 31. Change in output voltage for different harmonics as more CoFeSiB M1 fibers are added to the sample.

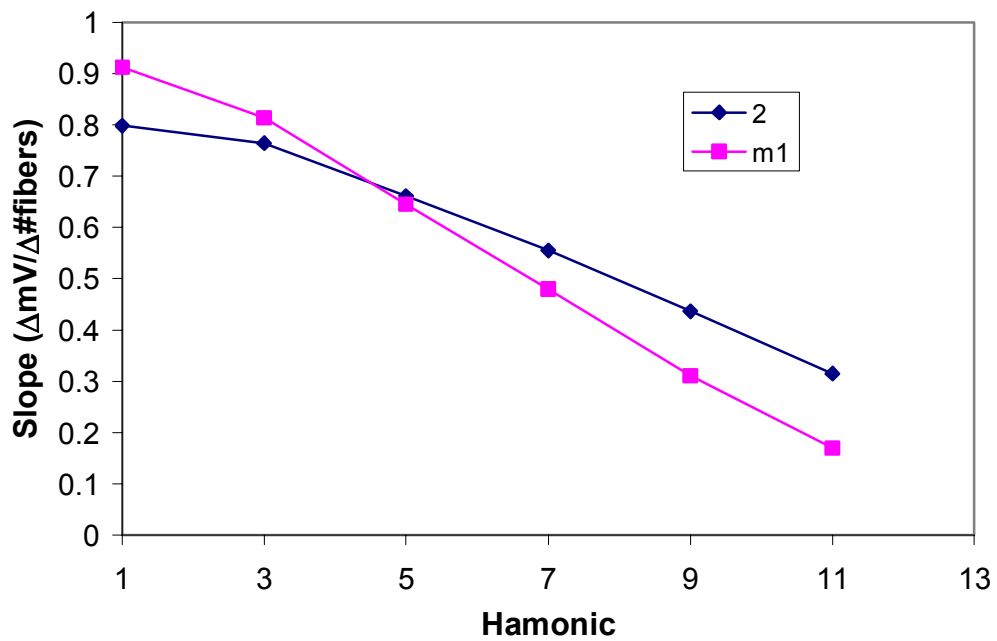


Figure 32. Comparison of two different CoFeSiB samples with respect to additional fibers (up to 4) in the sensor.

b. Fiber length

The effect of fiber length on sensor output was first modeled by finite element analysis and then the experimental results were compared. Figure 33 shows how the length of a fiber positioned in the center of the sensor should change the average magnetic field felt by the sensing coil. Until the length of the fiber reaches the length of the outer coil (sensing) it has a linear relationship for length to output, while for longer fibers the average output is a constant.

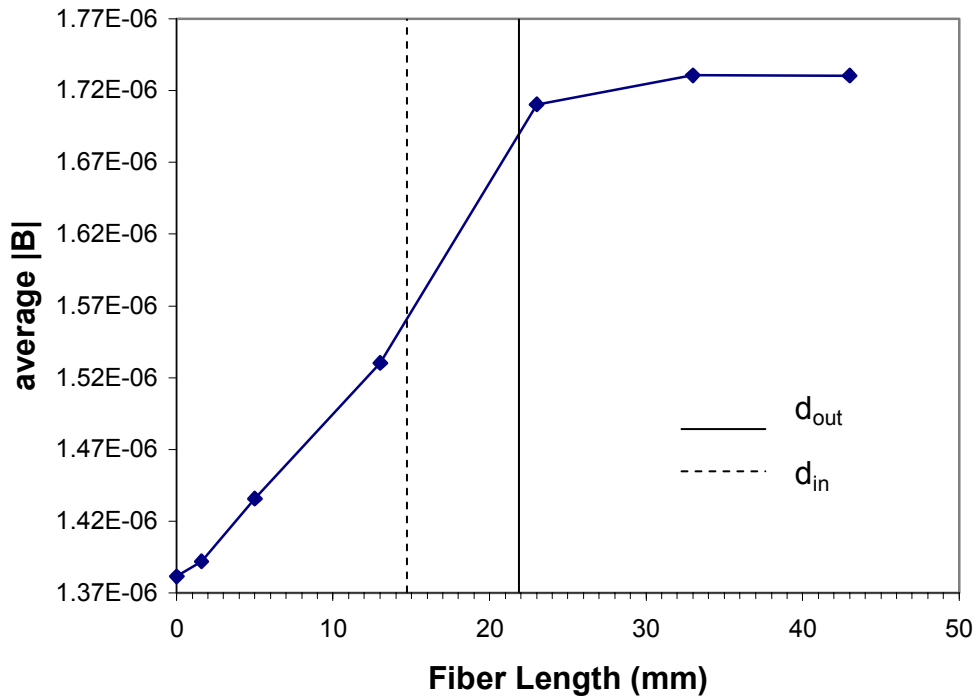


Figure 33. Change in magnetic field at the sensing coil as fiber sample length changes. (D_{in} = length of driving coil D_{out} = length of sensing coil)

Figures 34 and 35 are the experimental results from using different lengths of CoFeSiB samples in the sensor. It is seen that both designations fit the model very well suggesting that the other fibers will follow this same pattern.

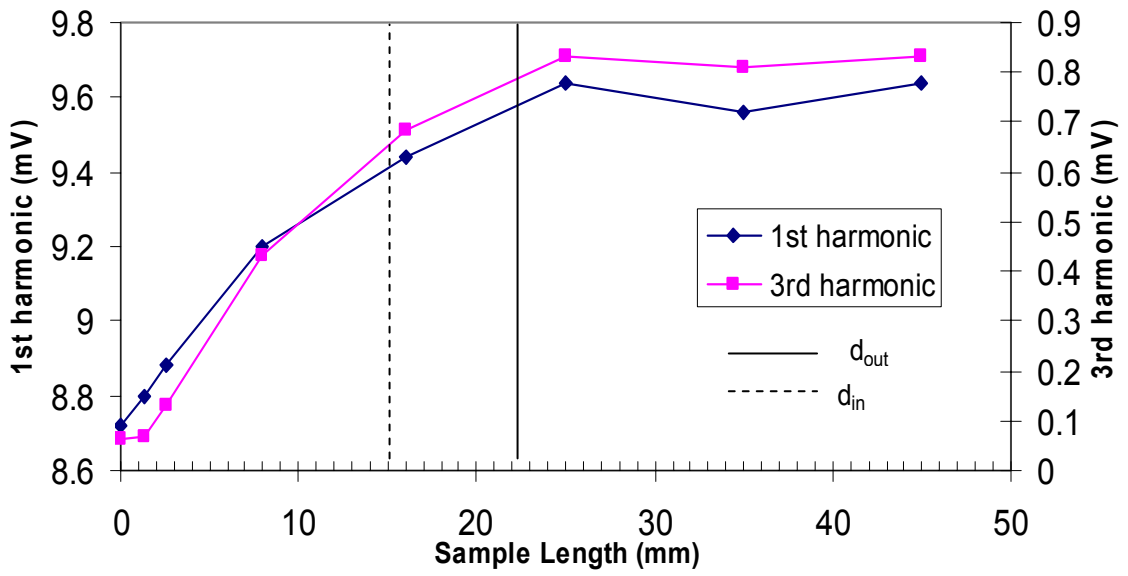


Figure 34. Change in voltage output with respect to sample length for CoFeSiB 2.

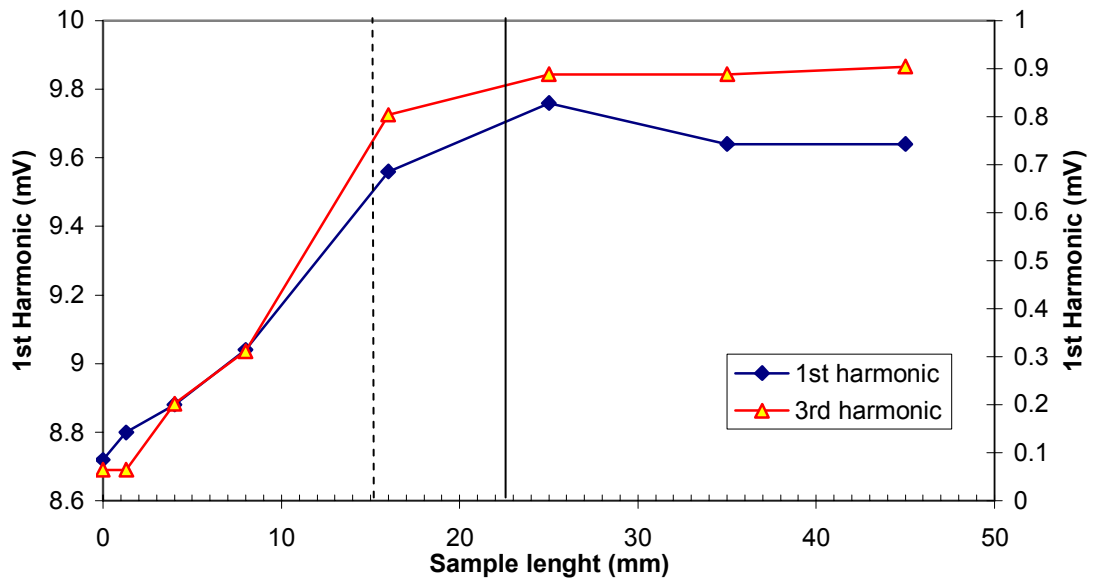


Figure 35. Change in voltage output with respect to changing sample length for M1 CoFeSiB.

D. Mechanical and magnetic coupling

Coupling of the mechanical properties to magnetic properties is very important to the development of GCAF based devices. This section looks at how the harmonic outputs depend on the tension and torsion in the sample as well as how the glass coating changes these magnetic properties. The property that the sensor is most dependent on is the magnetic permeability of the material as stated earlier. In this capacity a tensile load cell with a GCAF as the sensor core material was constructed. With further evaluation of the material (shear modulus) it will be easy to create a calibrated torsion sensing device.

1. Tension

Four different CoFeSiB GCAF were used in the sensor to provide a load cell function. The output voltage of different harmonics was calibrated against the hanging weight placed on the fiber to give the calibration curves seen in Figure 36. The same test was also performed on the G-R fibers which permitted the calculation of the stress relieved on the metal core by glass removal. Table 8 gives calibration factors for all 4 fibers with and without the glass coating and the R^2 values for each calibration showing that the relationship is indeed linear. The primary harmonic is assumed to display a similar pattern. However, due to the output of the signal analyzer only giving 3 significant figures the output voltages for the primary harmonic cannot be measured precisely. This makes quantitative measurements using the higher output harmonics difficult.

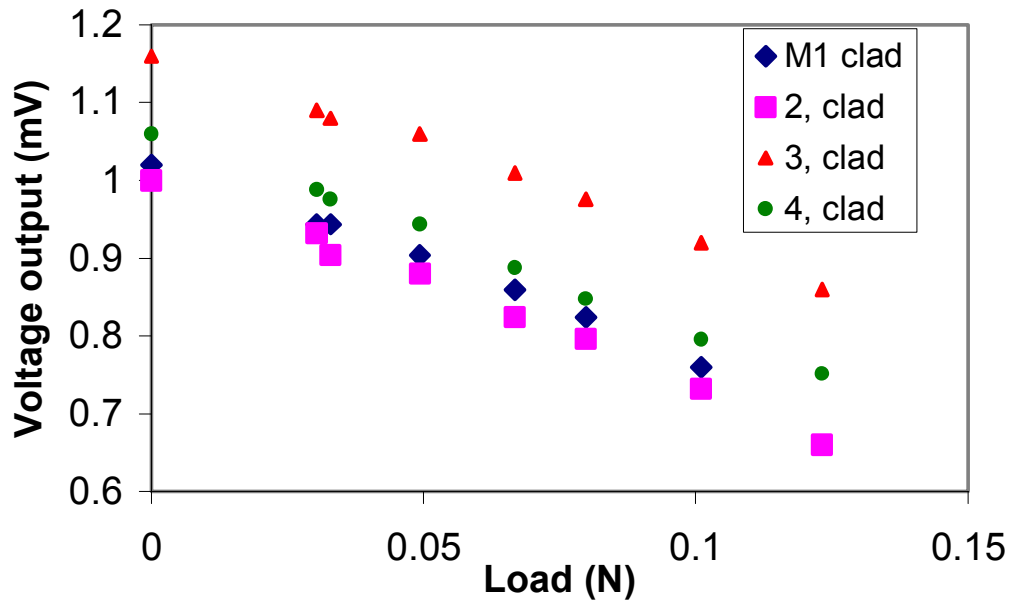


Figure 36. CoFeSiB fibers calibration curves for 3rd harmonic to be used use as a load cell.

Table VIII Calibration Data for CoFeSiB Fibers as a Load Cell in the Sensor
(Load(N)=output voltage (mV) of harmonic x slope + intercept)

Harmonic	slope	intercept	Rsqr	Harmonic	slope	intercept	Rsqr
M1 clad				M1 core			
3	-0.39338	-0.40302	0.99649	3	-0.55459	-0.67519	0.990442
5	-0.2353	-0.14389	0.998985	5	-0.30201	-0.31184	0.975006
7	-0.21139	-0.10448	0.993242	7	-0.22099	-0.23799	0.961156
2, clad				2, Core			
3	-0.36583	-0.36808	0.994199	3	-0.38014	-0.45206	0.961497
5	-0.22082	-0.14867	0.99816	5	-0.2552	-0.25182	0.978312
7	-0.20417	-0.12121	0.975247	7	-0.18604	-0.19814	0.963602
3, clad				3,Core			
3	-0.41339	-0.48188	0.994516	3	-0.57971	-0.77782	0.926588
5	-0.25624	-0.19078	0.998867	5	-0.30387	-0.34872	0.967882
7	-0.22565	-0.13373	0.992068	7	-0.2238	-0.26341	0.969106
4,clad				4,Core			
3	-0.388	-0.41215	0.99645	3	-0.46874	-0.61237	0.968994
5	-0.24519	-0.15883	0.998211	5	-0.25828	-0.27886	0.966135
7	-0.23624	-0.11759	0.984903	7	-0.19033	-0.21145	0.96872

Figure 37 shows the slope of the calibration curves for the 3rd 5th and 7th harmonics exhibited by A-R and G-R fibers. The largest difference in the slopes occurs at lower harmonics where the CoFeSiB M1, 3 and 4 G-R fibers have greater slopes than their A-R counterparts. The slope for CoFeSiB 2 is essentially unaffected by glass removal.

During testing it was found that the maximum weight each harmonic could sense was found to vary. The lower harmonic oscillations could sense heavier weights than the higher harmonics. Figure 38 shows this behavior. The maximum weight that each harmonic can sense scales linear for all of the compositions. With this linearity it is possible to predict how the primary harmonic should behave and the maximum weight the primary harmonic can measure.

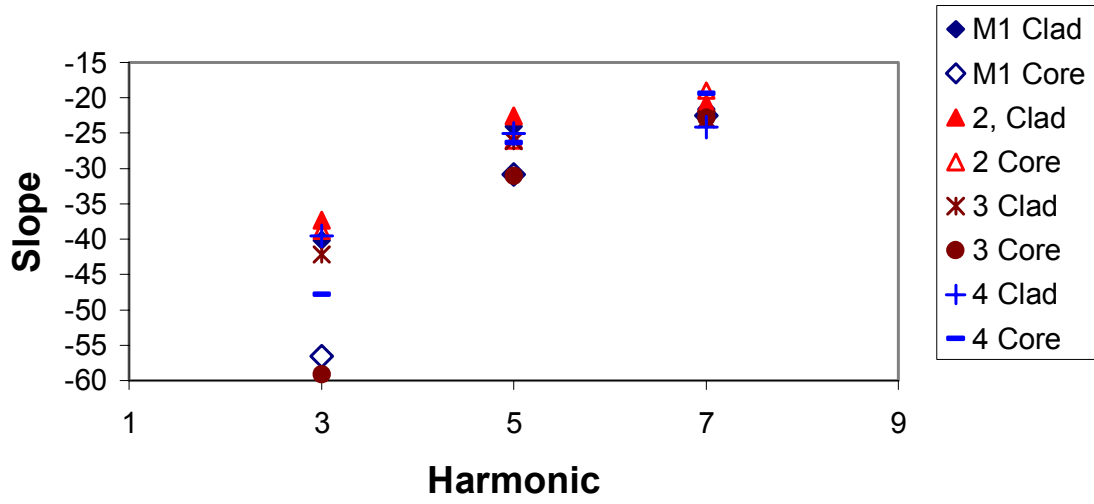


Figure 37. Changes in slope of CoFeSiB before (clad) and after (core) Glass removal for different harmonics.

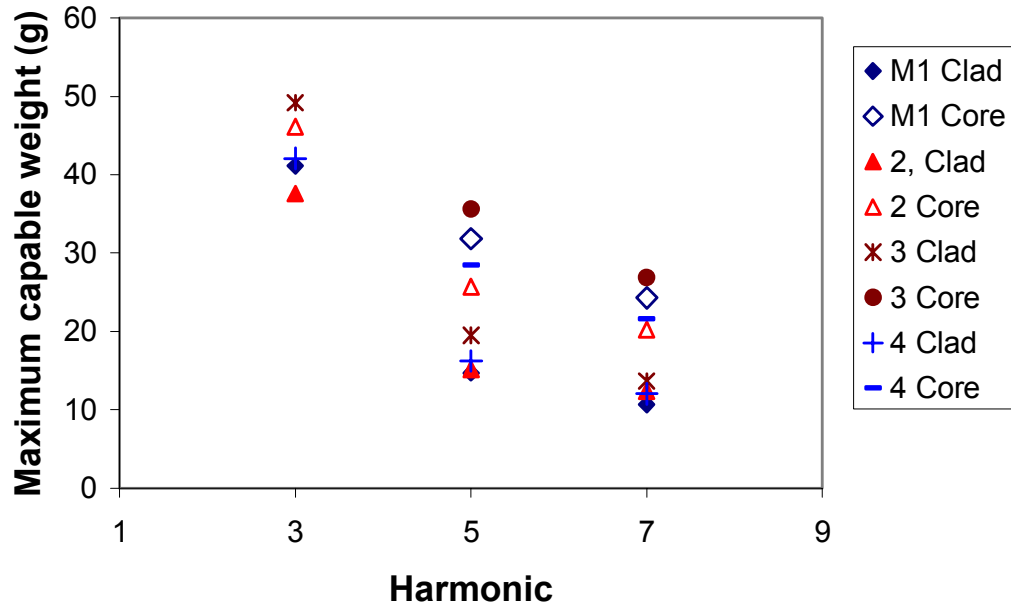


Figure 38. Maximum amount of weight that can be sensed on a specific harmonic and fiber type.

2. Torsion

The harmonic output under torsion was only measured for G-R samples since the glass cladding failed in shear, causing the fiber to slip out of the sensor. Figure 39 shows the relationship of harmonics 3, 5 and 7 to the number of turns placed on the fiber. It can be seen that the harmonic output of these harmonics increased but reached a limit as the torsion stress was increased. The 1st harmonic decreases in intensity as the torsion is increased. The decrease is assumed to mirror the increase that the higher harmonics show i.e. decrease to a certain point and level off. The exact values and shape of the primary harmonic as a function of torsion are not known due to the same argument given in the tension section about the preciseness of the primary harmonic measurement (large output voltage). However, the decrease in output is significant enough to be a real effect.

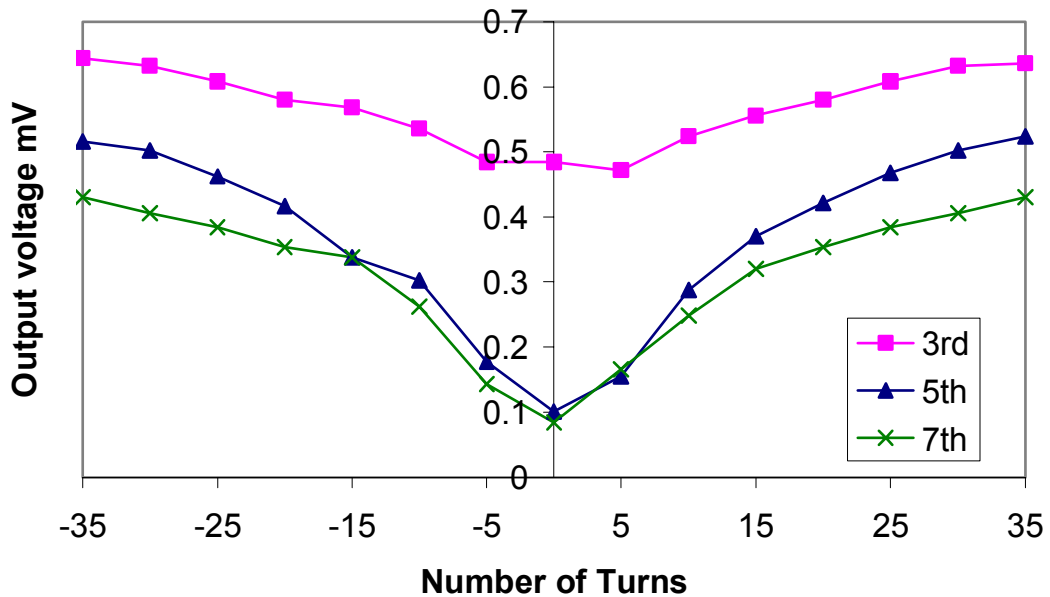


Figure 39. Effect of torsional stress on harmonic response of G-R CoFeSiB M1.

3. Stress relief

As stated in section 1 on tension, it is possible to calculate the stress relieved from the metal core by the removal of the glass cladding by comparing the calibration curves for a sample with and without its cladding. This is possible by looking at the harmonic output of the A-R fiber without any load and comparing it to the calibration curve of the

G-R fiber. Assuming that the harmonic component is only influenced by the force applied in the axial direction, this reasoning works. If the harmonic is also influenced by radial compression the result will be a slight overestimate or underestimate depending on how radial compression influences the harmonics. The process is shown graphically in figure 40 where the arrow indicates the amount of force placed on the core by the glass cladding. Table 9 shows the values of stress relieved calculated by this method for the four CoFeSiB designations.

Figure 41 shows the calculated axial stresses placed on the metal core by the glass cladding using formulas 9 and 14 for Rongved and Chiriac respectfully. The third set of data is the measured stress release from table 9. It is seen that the relieved stress does fall between the two calculated stresses. It must also be noted that the measured stress release is not necessarily the total stress on the fiber. There may be unreleased residual stresses due to rapid cooling and fictive temperature effects.

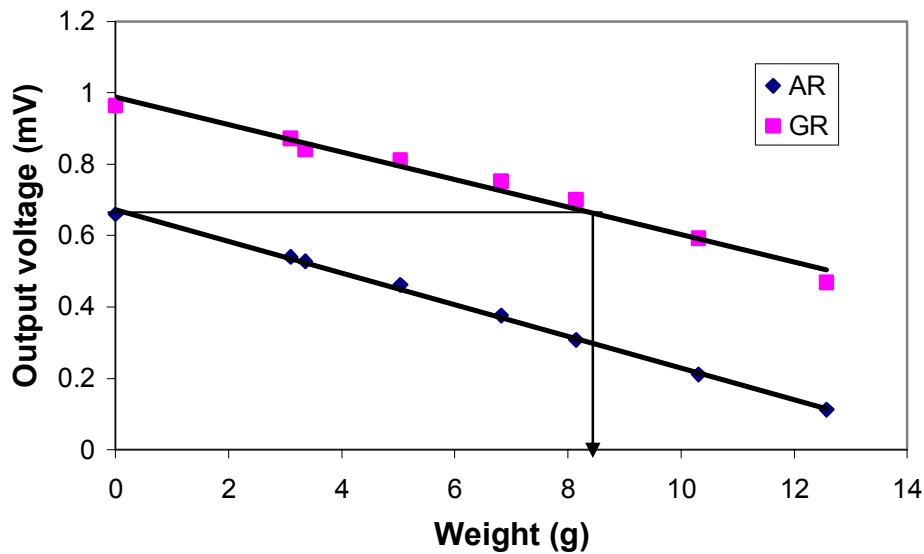


Figure 40. Calculating relieved stress when glass cladding is removed (example uses CoFeSiB 2 5th harmonic output).

Table IX Stress Relieved by the Removal of the Glass Coating for CoFeSiB Fibers

Designation	d_w (μm)	Weight (g)	Force (N)	Stress MPa
M1	24	11.09	0.11	240.38
2	24	7.97	0.08	172.67
3	23	11.17	0.11	263.56
4	25	11.62	0.11	232.06

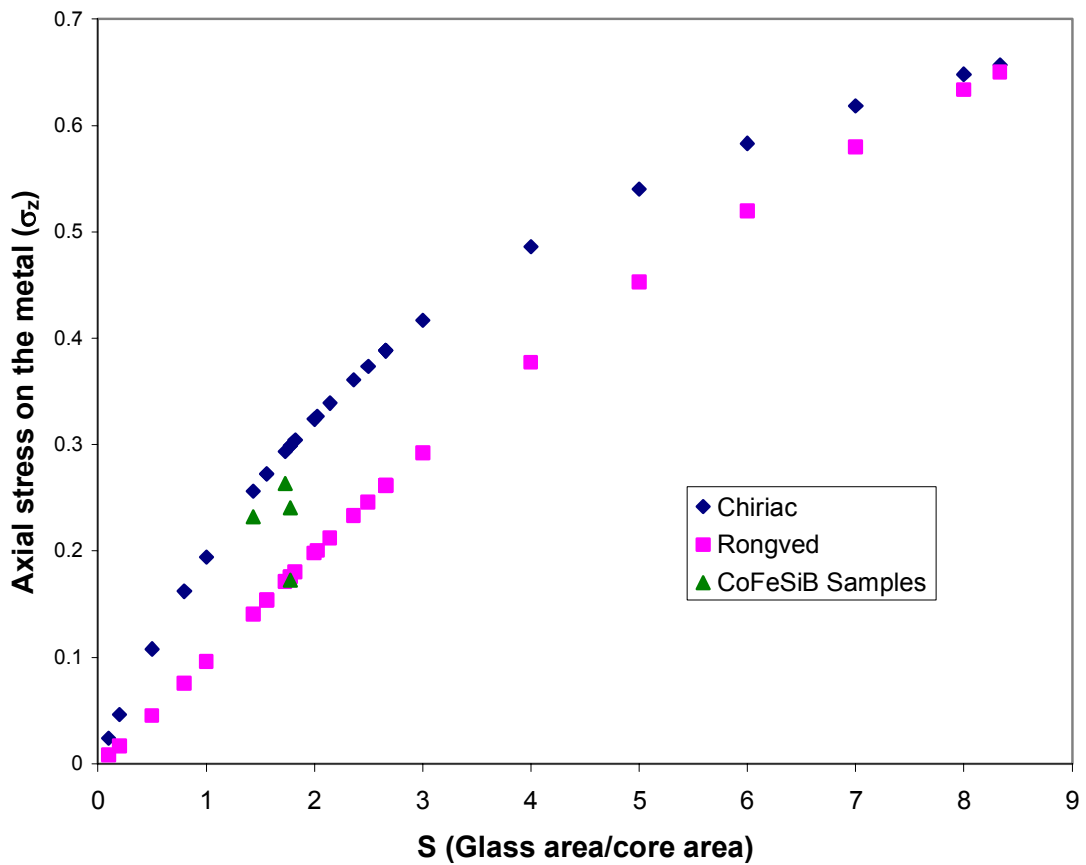


Figure 41. Axial stress on the metal core as a function of area ratio using Chiriac and Rongved's formulas.

IV SUMMARY AND CONCLUSIONS

- Mechanical properties of glass-coated metal fiber with different metal compositions CoFeSiB, CoFeNiSiB, and FeSiB were measured.
- Tensile strengths and Elastic modulus were measured with and without the glass coating present. Strengths on the order of 1-1.5 GPa were found for as-received GCAF and strengths on the order of 2 to 4 GPa have been found for the glass-removed fibers.
- The glass coating on the GCAF can fail in three ways, with the core, slowly as the core stretches, or fast fracture at a specific stress. CoFeSiB fibers experience the slow glass fracture while CoFeNiSiB and FeSiB experience both fast glass fracture and catastrophic failure. Fast glass fracture is limited to GCAF with high glass volume to core volume ratios. GCAF with thicker glass coatings can have improved ultimate failure strengths if the glass is pristine condition. This added benefit comes from the glass being in compression and the glass has a greater portion of the applied load than the internal metal core.
- The elastic modulus of the GCAF fall between 68 and 98 GPa which is 10 to 20% lower than the values calculated from a composite argument. The lower values are a result of imperfect bonding between the glass and the metal. Elastic modulus of the G-R fibers ranges from 120GPa to 180 GPa and depends on composition and the thickness of the metal fiber. Thinner fiber diameters tend to have a higher elastic modulus.
- The tensile strength of GCAF decreased 10 to 40% after crystallization depending on composition and the thickness of the glass coating. The tensile strength of samples with a thicker glass coating was less sensitive to devitrification of the metal core.
- A sensor was designed to observe the waveform and the harmonic components that each GCAF produced under a magnetic field. It is shown that the magnetic permeability of the CoFeSiB and CoFeNiSiB compositions was influenced by the

stress induced by the glass coating as well as tension and torsion forces. Tension placed axially on GCAF or the metal core decreased the permeability and the harmonic oscillations of the fibers. Torsion seems to decrease the permeability of the fibers however the harmonic components increase under tension. This change in permeability allowed the GCAF to be used in conjunction with a sensing device to function as a load cell or torsion cell. Calibration curves were made for four different CoFeSiB compositions for use as a load cell.

- The axial stress relieved on the metal core from the removal of the glass cladding was calculated from sensor measurements and found to be between 180 and 250MPa depending on the GCAF. These numbers were then compared against the calculated core stress from the forming process and seen to fall between the values calculated from Ronglev and Chiriac.
- The effects of fiber length and the multiple fibers were also looked at for future reference and possible device applications. Fiber length only influences the sensor if the length fiber being tested is less than the sensing coil. Once the fiber length exceeds the length of the sensing coil, the sensor output is constant. Multiple fibers change the sensor output linearly where higher harmonics are influenced more than lower harmonics.

V FUTURE WORK

This thesis starts to explore the mechanical properties of GCAF. The potential for fibers made using different glass coatings or core materials is large. More work should be done on manufacturing GCAF using different glass compositions and finding the mechanical relationships between the glass and the metal. Understanding the glass to metal bonding that occurs during the fiber forming process could possibly lead to fibers with better reinforcing properties or higher toughness.

A load cell was demonstrated in the thesis it would not be difficult to produce a better more cost effective device. The potential applications using the high cobalt fibers in mechanical load cells are immense. More experiments connecting the magnetic properties of GCAF to mechanical properties will generate new useful devices.

REFERENCES

1. H. Wiesner and J. Schneider, "Magnetic Properties of Amorphous Fe-P Alloys Containing Ga, Ge, and As," *Phys. Status Solidi A.*, **26** [1] 71-5 (1974).
2. G.F. Taylor, "A Method of Drawing Metallic Filaments and a Discussion of their Properties and Uses," *Phys. Rev.*, **23** [5] 665-0 (1924).
3. I. Ohnaka, T. Fukusako, and T. Ohmichi, "Production of Metal Filament by In-rotating-water Spinning Method," *J. Jpn. Inst. Met.*, **45** [7] 751-8 (1981).
4. H. Chiriac and T.A. Ovari, "Amorphous Glass-covered Magnetic Wires: Preparation, Properties, Applications," *Prog. Mater. Sci.*, **40** [5] 333-407 (1996).
5. V.S. Larin, A.V. Torcunov, A. Zhukov, J. Gonzalez, M. Vazquez, and L. Panina, "Preparation and Properties of Glass-coated Microwires," *J. Magn. Magn. Mater.*, **249** [1-2] 39-45 (2002).
6. H. Warlimont, "Amorphous Metals Driving Materials and Process Innovations," *Mater. Sci. Eng., A*, **304-306**, 61-7 (2001).
7. W.D. Callister, *Materials Science and Engineering an Introduction*, 4th ed.; pp. 520-21. John Wiley & Sons, New York, 1997.
8. L. Rongved, C.R. Kurjian, and F.T. Geyling, "Mechanical Tempering of Optical Fibers," *J. Non-Cryst. Solids*, **42** [1-3] 579-84 (1980).
9. A.K. Varshneya, D. Varshneya, and V. Jain, "On "Mechanical Tempering of Optical Fibers"," *J. Non-Cryst. Solids*, **93**, 215-6 (1987).
10. H. Chiriac, T.A. Ovari, and G. Pop, "Internal Stress Distribution in Glass-covered Amorphous Magnetic Wires," *Phys. Rev.*, **52** [14] 104-13 (1995).
11. H. Chiriac, E. Hristoforou, M. Neagu, and F. Borza, "Force Measurements Using Fe-rich Amorphous Wire as Magnetostrictive Delay Line," *Sens. Actuators*, **91** [1-2] 223-5 (2001).
12. H. Chiriac, E. Hristoforou, M. Neagu, I. Darie, and G. Lionis, "Torsional and Tensile Stress Dependence in Amorphous Magnetic Wires," *Sens. Actuators*, **59** [1-3] 79-83 (1997).

13. E. Hristoforou, C. Tsomokou, H. Chiriac, M. Neagu, and V. Nagacevschi, "Improving the Magnetostrictive Delay Line Resolution," *Sens. Actuators*, **59** [1-3] 84-8 (1997).
14. A. Zhukov, "Glass-coated Magnetic Microwires for Technical Applications," *J. Magn. Magn. Mater.*, **242-245** [Part 1] 216-23 (2002).
15. H. Chiriac and T.-A. Ovari, "Magnetic Properties of Amorphous Glass-covered Wires," *J. Magn. Magn. Mater.*, **249** [1-2] 46-54 (2002).
16. L. Kraus, Z. Frait, K.R. Pirota, and H. Chiriac, "Giant Magnetoimpedance in Glass-covered Amorphous Microwires," *J. Magn. Magn. Mater.*, **254**, 399-403 (2003).
17. M. Vazquez, M. Knobel, M.L. Sanchez, R. Valenzuela, and A.P. Zhukov, "Giant Magnetoimpedance Effect in Soft Magnetic Wires for Sensor Applications," *Sens. Actuators*, **59** [1-3] 20-9 (1997).
18. M. Knobel and K.R. Pirota, "Giant Magnetoimpedance: Concepts and Recent Progress," *J. Magn. Magn. Mater.*, **242-245** [Part 1] 33-40 (2002).
19. H. Chiriac, T.A. Ovari, C.S. Marinescu, D. Menard, and P. Ciureanu, "Comparative Study of the Magnetic Behavior of Co-rich Amorphous Fibers and Amorphous Glass-Covered Wires," *J. Magn. Magn. Mater.*, **169** [1-2] 159-81 (1999).
20. "Tensile Strength and Young's Modulus for High-Modulus Single-Filament Materials," ASTM Standard 3379-75. 1990 Annual Book of ASTM Standards, Vol. 15.01. American Society for Testing and Materials, West Conshohocken, PA, 1990.
21. I.M. Daniel and O. Ishai, *Engineering Mechanics of Composite Materials*; pp. 300-8. Oxford University Press, New York, 1994.
22. R.H. Doremus, *Glass Science*, 2nd ed. John Wiley & Sons, New York, 1994.
23. C. Hison, V. Iannotti, G. Ausanio, C. Luponio, and L. Lanotte, "A Magnetoelastic Amorphous Ribbon in a Silicone Sheath as Stress Sensor and Self Indicator of Strain Threshold," *Sens. Actuators*, **106** [1-3] 164-7 (2003).
24. D. Meeker, Finite Element Magnetic Method, [Computer Program] Accessed on: March, 2004. Available at <<http://femm.foster-miller.com>>.